

FINAL TECHNICAL REPORT - March, 2002

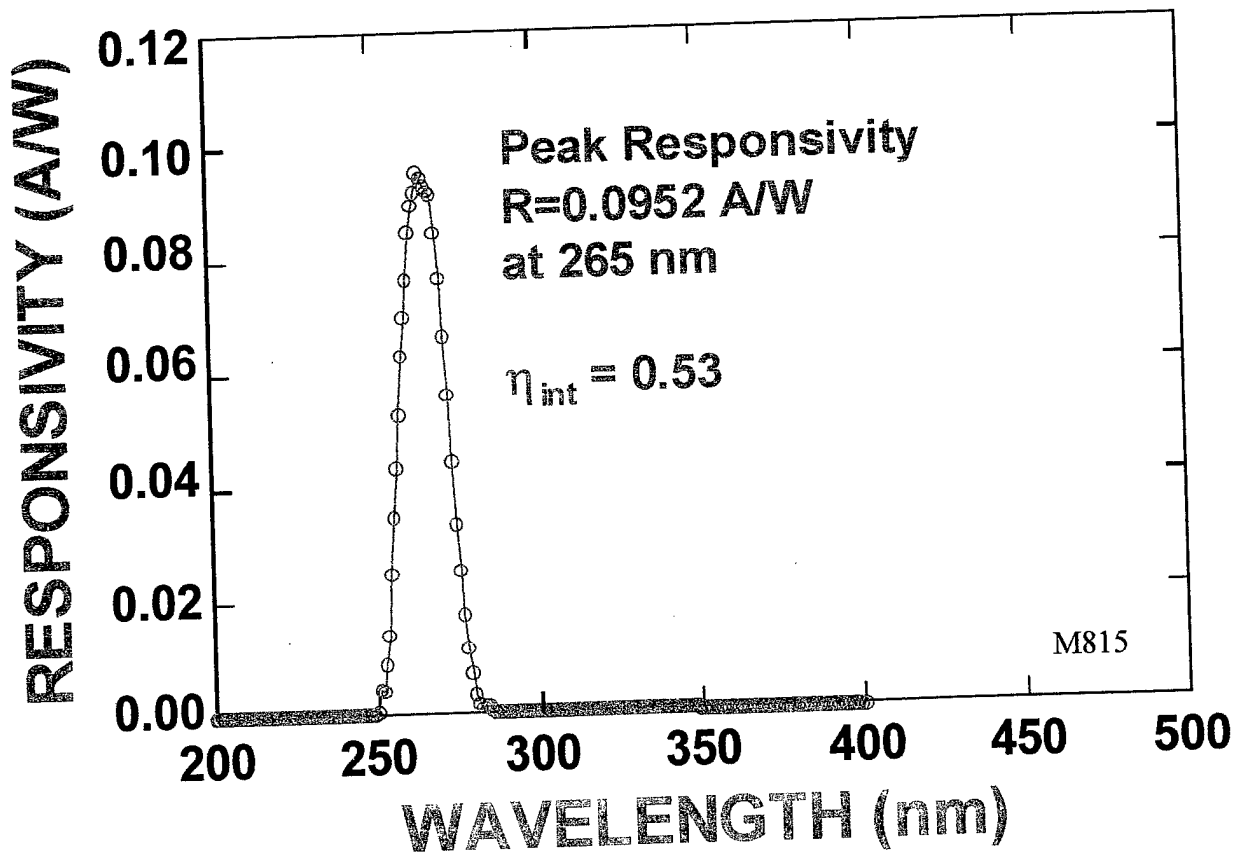
CONTRACT DAAG19-99-1-0010  
(March, 1999 - February, 2002)

**Development of High-Sensitivity Nitride Solar-Blind  
Detectors and Detector Arrays Using Low-  
Dislocation-Density Nitride Surfaces**

DARPA Solar Blind Detector Program  
Edgar Martinez, DARPA Program Manager

J.F. Schetzina

J.F. Schetzina, Principal Investigator  
North Carolina State University



20030227 116

## REPORT DOCUMENTATION PAGE

Form Approved  
OMB NO. 0704-0188

Public Reporting burden for this collection of information is estimated to average 1 hour per response, including the time for reviewing instructions, searching existing data sources, gathering and maintaining the data needed, and completing and reviewing the collection of information. Send comment regarding this burden estimates or any other aspect of this collection of information, including suggestions for reducing this burden, to Washington Headquarters Services, Directorate for Information Operations and Reports, 1215 Jefferson Davis Highway, Suite 1204, Arlington, VA 22202-4302, and to the Office of Management and Budget, Paperwork Reduction Project (0704-0188) Washington, DC 20503.

1. AGENCY USE ONLY (Leave Blank)		2. REPORT DATE <b>March 29, 2002</b>		3. REPORT TYPE AND DATES COVERED <b>3-01-99 - 2-28-02</b> <b>FINAL REPORT</b>	
4. TITLE AND SUBTITLE <b>Development of High-Sensitivity Nitride Solar-Blind Detectors Using Low-Density Nitride Surfaces</b>				5. FUNDING NUMBERS <b>DAAD19-99-1-0010</b>	
6. AUTHOR(S) <b>J. F. Schetzina</b>					
7. PERFORMING ORGANIZATION NAME(S) AND ADDRESS(ES) <b>North Carolina State University Office of Sponsored Programs - Box 7514 Raleigh, NC 27695-7514</b>				8. PERFORMING ORGANIZATION REPORT NUMBER	
9. SPONSORING / MONITORING AGENCY NAME(S) AND ADDRESS(ES) <b>U. S. Army Research Office P.O. Box 12211 Research Triangle Park, NC 27709-2211</b>				10. SPONSORING / MONITORING AGENCY REPORT NUMBER <b>39999-EL</b>	
11. SUPPLEMENTARY NOTES The views, opinions and/or findings contained in this report are those of the author(s) and should not be construed as an official Department of the Army position, policy or decision, unless so designated by other documentation.					
12 a. DISTRIBUTION / AVAILABILITY STATEMENT  Approved for public release; distribution unlimited.			12 b. DISTRIBUTION CODE		
13. ABSTRACT (Maximum 200 words)  <b>This work explored the application of III-V nitride semiconductors for optical detectors in the ultraviolet (UV) region of the electromagnetic spectrum. Metalorganic vapor phase epitaxy was used to synthesize thin film p-i-n photodiode structures on double side polished sapphire substrates. These structures were fabricated into photodiode devices using generally accepted techniques for dry etching and p and n-contact metallizations. Test devices were characterized which demonstrated quantum efficiencies as high as 80%, along with extremely low dark currents; resulting in photodiode spectral detectivities as large as <math>6 \times 10^{13} \text{ cmHz}^{1/2} \text{W}^{-1}</math>. Devices were designed and demonstrated for a series of detection regions ranging from 365 nm to 250 nm. Photodiode arrays were also fabricated and flip-chip bonded to silicon readout integrated circuits (ROICs) to form the basis of visible-blind and solar-blind UV digital cameras. These UV-specific digital arrays were tested using focal plane array hardware and software obtained from SE-IR, Inc.</b>					
14. SUBJECT TERMS				15. NUMBER OF PAGES <b>59</b>	
				16. PRICE CODE	
17. SECURITY CLASSIFICATION OR REPORT <b>UNCLASSIFIED</b>		18. SECURITY CLASSIFICATION ON THIS PAGE <b>UNCLASSIFIED</b>		19. SECURITY CLASSIFICATION OF ABSTRACT <b>UNCLASSIFIED</b>	
				20. LIMITATION OF ABSTRACT <b>UL</b>	

NSN 7540-01-280-5500

Standard Form 298 (Rev.2-89)  
Prescribed by ANSI Std. Z39-18  
298-102

Enclosure 1

**MASTER COPY:** PLEASE KEEP THIS "MEMORANDUM OF TRANSMITTAL" BLANK FOR REPRODUCTION PURPOSES. WHEN REPORTS ARE GENERATED UNDER THE ARO SPONSORSHIP, FORWARD A COMPLETED COPY OF THIS FORM WITH EACH REPORT SHIPMENT TO THE ARO. THIS WILL ASSURE PROPER IDENTIFICATION. NOT TO BE USED FOR INTERIM PROGRESS REPORTS; SEE PAGE 2 FOR INTERIM PROGRESS REPORT INSTRUCTIONS.

**MEMORANDUM OF TRANSMITTAL**

U.S. Army Research Office  
ATTN: AMSRL-RO-BI (TR)  
P.O. Box 12211  
Research Triangle Park, NC 27709-2211

Reprint (Orig + 2 copies)       Technical Report (Orig + 2 copies)  
 Manuscript (1 copy)       Final Progress Report (Orig + 2 copies)  
     Related Materials, Abstracts, Theses (1 copy)

CONTRACT/GRANT NUMBER: **DAAD19-99-1-0010**

REPORT TITLE: **Development of High-Sensitivity Nitride Solar-Blind Detectors Using Low-Density Nitride Surfaces**

is forwarded for your information.

SUBMITTED FOR PUBLICATION TO (applicable only if report is manuscript):

Sincerely,



FINAL TECHNICAL REPORT - March, 2002

CONTRACT DAAG19-99-1-0010  
(March, 1999 - February, 2002)

## **Development of High-Sensitivity Nitride Solar-Blind Detectors and Detector Arrays Using Low-Dislocation-Density Nitride Surfaces**

**DARPA Solar Blind Detector Program**  
**Edgar Martinez, DARPA Program Manager**

**J.F. Schetzina, Principal Investigator**  
**North Carolina State University**

### **Abstract**

This work explored the application of III-V nitride semiconductors for optical detectors in the ultraviolet (UV) region of the electromagnetic spectrum. Metal-organic vapor phase epitaxy was used to synthesize thin film p-i-n photodiode structures on double side polished sapphire substrates. These films were characterized for optical, electrical and structural properties. These structures were fabricated into photodiode devices using generally accepted techniques for dry etching and p and n-contact metallizations. Test devices were characterized which demonstrated quantum efficiencies as high as 80%, along with extremely low dark currents; resulting in photodiode spectral detectivities as large as  $6*10^{13} \text{ cmHz}^{1/2}\text{W}^{-1}$ . Devices were designed and demonstrated for a series of detection regions ranging from 365 nm to 250 nm. Photodiode arrays were also fabricated and flip-chip bonded to silicon readout integrated circuits (ROICs) to form the basis of visible-blind and solar-blind UV digital cameras. These UV-specific digital arrays were tested using focal plane array hardware and software obtained from SE-IR, Inc.

## TABLE OF CONTENTS

1. INTRODUCTION	4
1.1 Introduction to III-V Materials	4
1.2 Properties and Applications of III-V Nitride Materials	4
1.3 Purpose of Research Program	7
2. EXPERIMENTAL DETAILS AND PROCEDURES	5
2.1 Crystal Growth	5
2.2 Materials Characterization Experiments	7
2.3 Device Fabrication and Testing Experiments	7
2.3.1 Discrete Photodiodes	7
2.3.2 Photodiode Arrays	13
2.4 SE-IR Digital Camera	21
2.4.1 Basic Operating Characteristics	21
2.4.2 Diode Array Statistics	26
2.5 UV Imaging Techniques	27
3. RESULTS AND DISCUSSION	30
3.1 Characterization of Visible-Blind UV Photodiodes	30
3.2 UV-Specific (320-365 nm) Digital Camera Based On	
128x128 Focal Plane Array of GaN/AlGaN p-i-n Photodiodes	33
3.3 Characterization of Solar-Blind AlGaN UV Photodiodes	36
3.4 Properties of 128x128 and 320x256 Solar-Blind	
Focal Plane Arrays of AlGaN UV Photodiodes	46
3.5 Diode Array Statistics	49

4. Summary	53
5. References	55

# 1 INTRODUCTION

## 1.1 Introduction to III-V Materials

The class of III-V semiconductor compounds has been studied since the beginning of the semiconductor industry. These materials are denoted III-V because one of the elements in the binary compound, the cation, comes from group III in the periodic table, and the other element, the anion, comes from group V in the periodic table. Of the III-V materials, GaAs, AlAs, and InP, as well as their alloys, have been studied most extensively. Devices made from these compounds are optically active from the greenish-yellow to the infrared regions of the spectrum.

## 1.2 Properties and Applications of III-V Nitride Materials

Interest in a subclass of the III-V compounds, the III-N semiconductors, has grown rapidly in recent years. The nitride materials GaN and AlN have bandgaps in the ultraviolet, 3.4 eV and 6.2 eV, respectively. InN has a bandgap of 1.9 eV, which falls in the red region of the spectrum. Therefore, alloys of these three materials can be optically active at wavelengths ranging from the red to the ultraviolet (Figure 1.1). This wide range makes the III-N compounds an obvious choice for use in optoelectronic devices such as light emitting diodes (LEDs), semiconductor lasers, and photodetectors. Currently, Nichia Chemical Industries has commercially available bright blue and green LEDs based on GaN/InGaN structures [1]. Nichia has also demonstrated a semiconductor laser based on InGaN/AlGaN/GaN that has an estimated lifetime of 10,000 hours operating under continuous wave conditions at room temperature. Other commercially available devices based on GaN and its

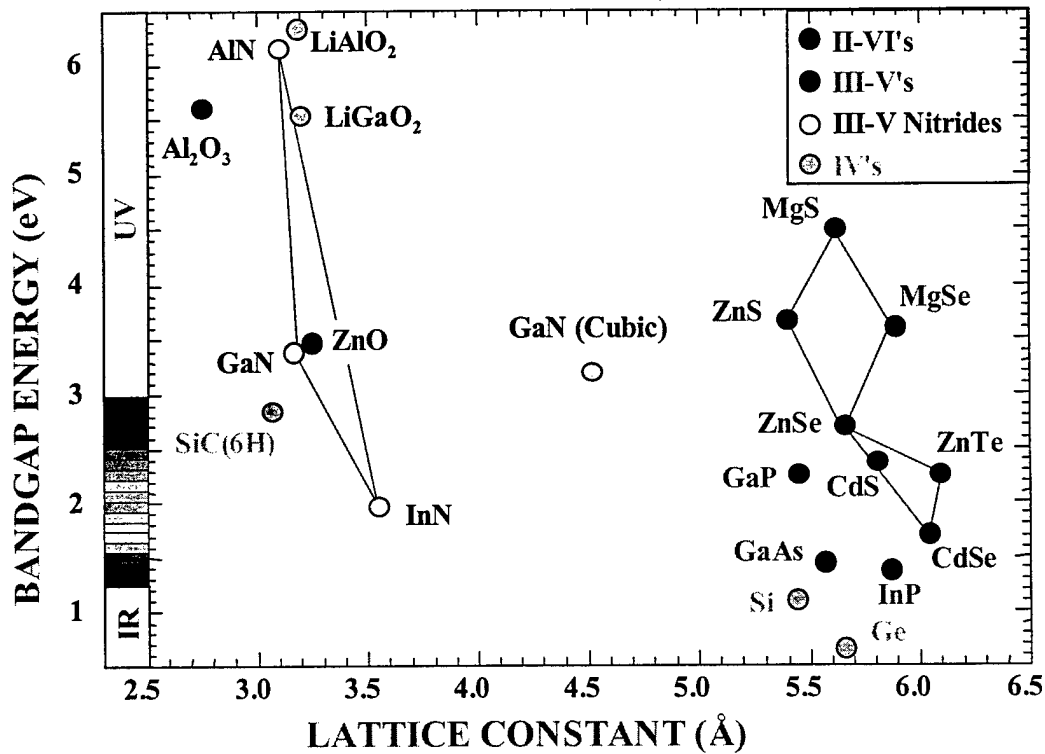


Figure 1.1 Bandgap versus lattice-constant for selected semiconductors.

alloys include blue and green LEDs made by Toyoda Gosei in Japan and Cree, Inc. in North Carolina.

The advantages of GaN and AlN over other III-V semiconductors in certain device applications include the physical and electrical stability of III-N materials at high temperatures. The melting points of both compounds are well above 2000°C, although they start to lose nitrogen from the lattice at temperatures above 600-700°C [3]. In most semiconductors the electrical properties of the material are a strong function of the temperature. Due to the wide bandgaps of GaN and AlN, higher temperatures are not as detrimental to the electrical properties as they would be for narrower gap materials like GaAs. In particular, the intrinsic carrier

concentration in GaN is so small that p-n junctions are viable at temperatures up to 500°C. For these reasons of stability, GaN and the alloy AlGaN are promising materials for high output microwave power devices.

However one of the most recent applications that has triggered considerable research in this field is UV photodetectors. These devices are discussed in detail in subsequent sections of this report. A photodetector is an optoelectronic device that absorbs optical energy and converts it to electrical energy. The electrical energy can be observed as photocurrent. There are three basic steps involved in the photodetection process: (1) absorption of optical energy; (2) transportation of photogenerated carriers across the absorption region; (3) carrier collection and generation of photocurrent, which flows through an external circuit. [1]

There are three main types of detectors: photoconductors, avalanche photodiodes, and p-i-n diodes. A photoconductor operates based on the principle of increase in conductivity of a specific region with excitation. This results in carriers being generated, which is collected by contacts and result in photocurrent.

Avalanche photodiodes are used in applications that require large gains. These diodes are operated very close to their breakdown voltages. When the carriers acquire enough energy they cause an ionizing collision to occur which in turn leads to the production of more carriers. This leads to carrier multiplication and thus results in a large gain.

Another type of detector that has been actively researched with III-V nitride is the p-i-n photodiode. It is a junction diode that has an undoped i region in between a p and an n region. The depletion layer is carefully controlled and absorbs all the

photogenerated carriers. Since p-i-n photodiodes don't have any internal gain the maximum internal quantum efficiency possible is 100%. All the devices discussed as part of this work are of the p-i-n type. The structure and behavior of these devices are discussed in the later sections of this report.

### **1.3 Purpose of Research Program**

This research program explored the application of III-V nitride semiconductors for optical detectors in the ultraviolet (UV) region of the electromagnetic spectrum. Specifically, this work involved the testing of both discrete UV photodetectors based on AlGaN p-i-n heterostructure photodiodes, and photodiode arrays that operate as radiation detectors in the UV. Two types of detectors and arrays were studied: Visible-blind devices that respond to UV radiation in the 300-365 nm region, and solar-blind devices that respond to UV light in the 240-285 nm region.

An important task of this work was the evaluation of UV photodiode arrays fabricated to form digital UV imaging devices. 32x32, 128x128 and 320x256 UV photodiode arrays were fabricated and flip-chip bonded to silicon readout integrated circuits (ROICs) to form the basis of visible-blind and solar-blind UV digital cameras. These UV-specific digital arrays were tested using focal plane array hardware and software obtained from SE-IR Corporation.

## 2 EXPERIMENTAL DETAILS AND PROCEDURES

### 2.1 Crystal Growth

The photodiode structures employed in the present work is shown schematically in Figure 2.1 and Figure 2.2. The visible-blind device consists of a base layer of n-AlGaN (~20% Al) followed by an undoped GaN layer and a p-GaN layer. The photodiode structure is deposited by MOVPE onto a polished sapphire wafer to permit illumination of the device through the substrate. As shown in the figure, the photodiode responds to UV light in the wavelength band from about 320 nm to 365 nm. At wavelengths shorter than 320 nm, the incoming light is absorbed in the thick AlGaN base layer and the junction is not illuminated. Likewise, the diode does not respond to wavelengths greater than 365 nm, since this corresponds to the optical absorption edge of GaN at 300K. By increasing the Al content of the base layer it is possible to increase the optical bandwidth of the diode's UV responsivity. Likewise, by adding Al to the top layers, it is possible to change the diode UV responsivity band to other wavelength regions in the UV. Thus, UV detectors that sense different UV "colors" are possible. The solar-blind device shown in Figure 2.2 consists of a base layer of n-AlGaN (64% Al) followed by an undoped AlGaN and an p-GaN layer having 146% Al. This structure is designed to respond to a narrow band of UV radiation in the 250-285 nm region of the spectrum.

Diode structures of the type shown were prepared by MOVPE both at North Carolina State University (NCSU) and at the Honeywell Technology Center using low-pressure, vertical-flow MOVPE reactors that employ high speed substrate rotation during film growth. The photodiode structures were deposited onto 2 in

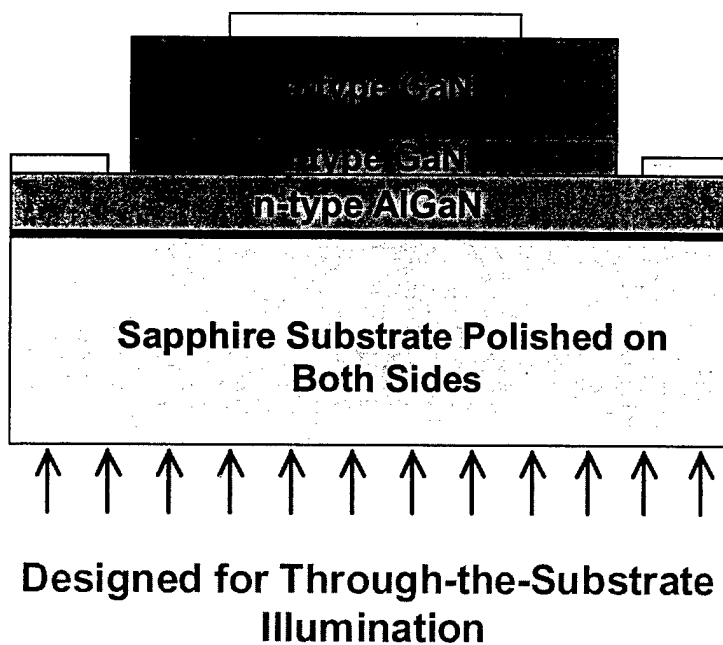


Figure 2.1 Visible-blind (300-365 nm) GaN/AlGaN heterostructure p-i-n photodiode.

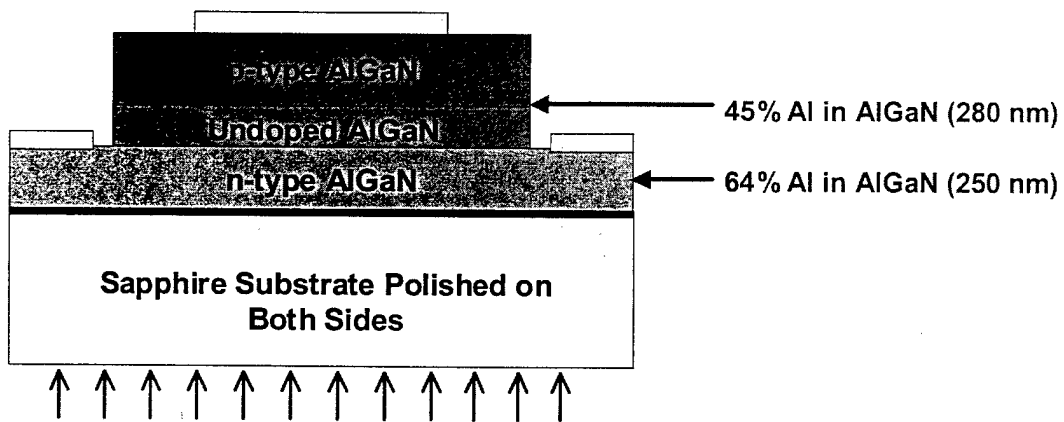


Figure 2.2 Solar-blind AlGaN heterostructure p-i-n photodiode.

diameter c-plane sapphire substrates. The growth was initiated by depositing a thin AlN buffer layer at 500-650 °C; all subsequent layers were grown at 1050-1080 °C.

## **2.2 Materials Characterization Experiments**

In order to optimize the above photodiode structures, a series of samples were grown under various combinations of growth temperatures, growth rates, and gas flow rates. Capacitance-voltage (C-V), optical absorption, photoluminescence and cathodoluminescence (CL) measurements were employed in this optimization procedure. In the case of the solar-blind detector structures, the n-type  $\text{Al}_{0.64}\text{Ga}_{0.36}\text{N}:\text{Si}$  base layer was initially optimized using C-V, CL and optical absorption measurements. The undoped  $\text{Al}_{0.45}\text{Ga}_{0.55}\text{N}$  active layer and p-type magnesium doped  $\text{Al}_{0.45}\text{Ga}_{0.55}\text{N}:\text{Mg}$  top layer of the device structure were then optimized with the aid of optical absorption and cathodoluminescence measurements.

## **2.3 Device Fabrication and Testing Experiments**

### **2.3.1 Discrete Photodiodes**

All device processing was completed using standard semiconductor processing techniques which included photolithography using appropriately-designed masks, reactive ion etching to define mesa structures, and metallizations to provide ohmic contacts to the n-type and p-type layers of the devices. Boron

trichloride ( $\text{BCl}_3$ ) was employed in the reactive ion etching chamber using photolithographically defined Ni masks to etch the  $200 \mu\text{m} \times 200 \mu\text{m}$  photodiode mesas. Etch rates of  $\sim 17.5 \text{ nm/sec}$  were obtained using  $\text{BCl}_3$  flow rates of 35 sccm at a chamber pressure of 30 mTorr and an RF power level of 100 W. Ni/Au and Ti/Al metallizations, followed by an anneal at  $600\text{-}700^\circ\text{C}$ , were employed to obtain p-type and n-type ohmic contacts, respectively.

Let us consider a p-n junction or p-i-n junction photodiode operating in the photovoltaic mode at zero bias [14]. The detector current responsivity  $R_\lambda$  is defined as the output current  $i_p$  produced by the detector divided by the diode illumination power  $P_\lambda$  at a given wavelength  $\lambda$ . That is,

$$R_\lambda = i_p / P_\lambda = q\eta/h\nu \quad (\text{A/W}) \quad (1)$$

where  $q$  is the electronic charge,  $\eta$  is the quantum efficiency,  $h$  is Planck's constant and  $\nu$  is the radiation frequency. Note that the responsivity  $R_\lambda$  varies inversely with the optical frequency  $\nu$ . As a consequence, maximum responsivities ( $\eta = 1$ ) in the UV are small -- ranging from  $R_\lambda = 0.294 \text{ A/W}$  at  $365 \text{ nm}$  to  $R_\lambda = 0.161 \text{ A/W}$  at  $200 \text{ nm}$  as shown in Figure 2.3.

An important figure of merit for a diode detector is the  $R_0A$  product, where  $R_0$  is the dynamic resistance of the diode at zero bias and  $A$  is the detector area. A large  $R_0A$  product is a necessary requirement for the detector to have a large detectivity  $D^*$ . That is, for the detector to be able to detect very low light levels. Figure 2.4 shows the spectral detectivity  $D^*$  for a number of different commercially-available detectors [15] that operate at wavelengths ranging from  $0.2 \mu\text{m}$  (UV) to  $12 \mu\text{m}$  (IR).

$\mu\text{m}$  (IR). It is seen from the figure that IR detectors display  $D^*$  values of  $10^7$  -  $10^{10}$   $(\text{cm Hz}^{1/2}\text{W}^{-1})$

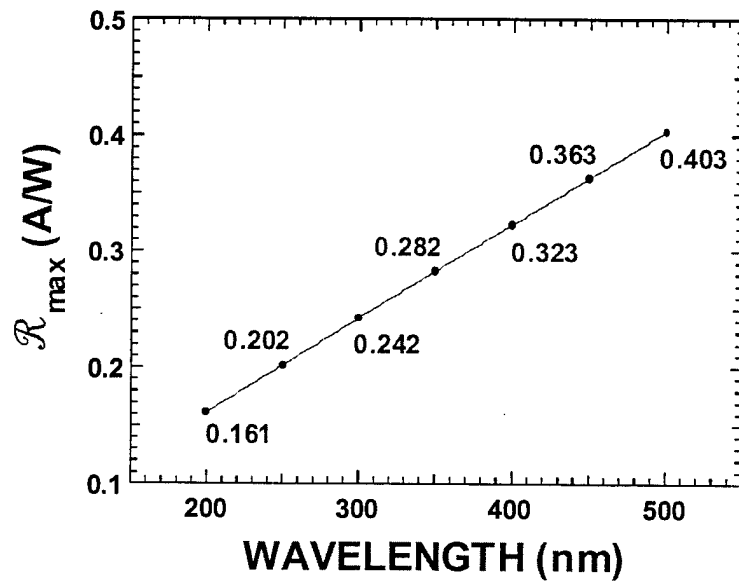


Figure 2.3 Maximum responsivity versus wavelength.

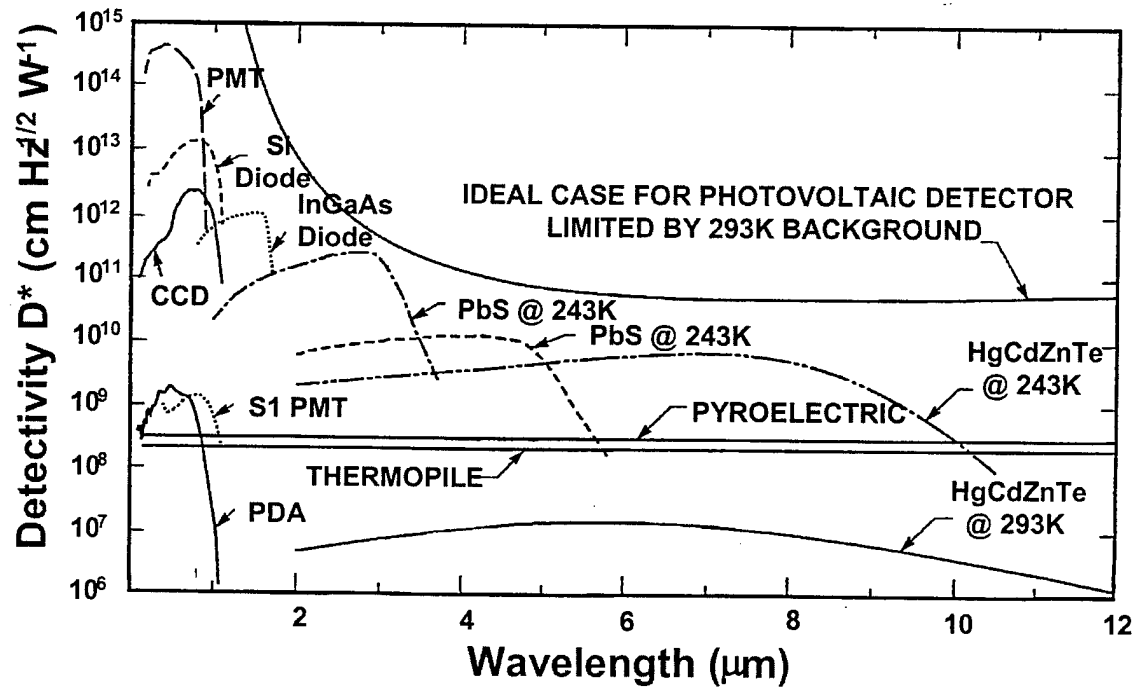


Figure 2.4 Detectivity  $D^*$  versus wavelength for selected photodetectors.

depending on the type of detector, its operating temperature, and the wavelength region for which it is designed. Detectors operating at shorter wavelengths generally display larger  $D^*$  values ranging up to  $D^* = 4 \times 10^{14} \text{ (cm Hz}^{1/2}\text{W}^{-1}\text{)}$  for a photomultiplier tube (PMT) operating at about 300 nm.

Figure 2.4 also shows the curve for an ideal photovoltaic detector limited by thermal background radiation from a 293K radiation source (the earth!!). A detector displaying  $D^*$  values that lie along this line is said to be background limited. A Background Limited Photodetector is often referred to as being a BLIP-limited detector, or as being BLIP-limited [14]. These detectors have the highest possible  $D^*$  values for a given wavelength when exposed to the earth's thermal radiation field. Note from the figure, that  $D^*$  values for a BLIP-limited detector become extremely large as the wavelength decreases into the UV. This is because a 293K black body radiation background contains virtually no UV radiation, so an extremely sensitive detector is required to be able to detect this near-zero thermal background from the earth.

The spectral detectivity  $D^*$  of a photodiode detector may be expressed as [14]

$$D^* = (q\eta/hv) [(4kT/R_0A) + 2q^2\eta\Phi_b]^{1/2} \text{ (cm Hz}^{1/2}\text{W}^{-1}\text{)}. \quad (3)$$

The first term in the bracketed quantity above ( $4kT/R_0A$ ) arises from thermal noise sources within the detector. The second term ( $2q^2\eta\Phi_b$ ) is due to the background radiation  $\Phi_b$  to which the detector is exposed. If the detector is limited by thermal noise, that is, if the thermal noise far exceeds the background radiation induced signal, then the detectivity becomes

$$D^* = (q\eta/h\nu) [(4kT/R_0A)]^{-1/2} = (q\eta/h\nu) (R_0A/4kT)^{1/2} \text{ (cm Hz}^{1/2}\text{W}^{-1}), \quad (4)$$

where  $k$  is Boltzmann's constant and  $T$  is the absolute temperature. Note that the detectivity  $D^*$  is directly proportional to  $(R_0A)^{1/2}$  when the detector is noise-limited. Thus, to develop very sensitive detectors it is essential that the detector noise sources be minimized so that  $R_0A$  is large. In the case of III-V nitrides, the extremely large density of dislocations represents a significant noise source. Therefore, dislocation reduction should have a very positive effect on the detectivity of nitride photodiodes.

If the second term in brackets of equation (3) above dominates, then the background signal determines  $D^*$ . In this case, the detectivity  $D^*$  is BLIP-limited and may be expressed as

$$D^*_{BLIP} = (q\eta/h\nu) [2q^2\eta\Phi_b]^{1/2} = (1/h\nu) (\eta/2\Phi_b)^{1/2} \text{ (cm Hz}^{1/2}\text{W}^{-1}). \quad (5)$$

The detectivity  $D^*$  may also be expressed in terms of the detector noise equivalent power NEP such that [14]

$$D^* = (A\Delta f)^{1/2}/\text{NEP} \text{ (cm Hz}^{1/2}\text{W}^{-1}), \quad (6)$$

where  $A$  is the detector area and  $\Delta f$  is the detector bandwidth. The noise equivalent power NEP is the power that corresponds to the incident rms optical power required such that the detector signal-to-noise ratio is one in a bandwidth of 1 Hz.

Spectral responsivity measurements were completed on selected discrete photodiodes. In these experiments a xenon lamp was employed as a UV source and the wavelengths were selected by a monochromator. The monochromator output was calibrated using a calibrated UV-enhanced Si photodiode and the data were

compiled with the aid of a computer. The experimental setup employed for these measurements is shown in Figure 2.5 below.

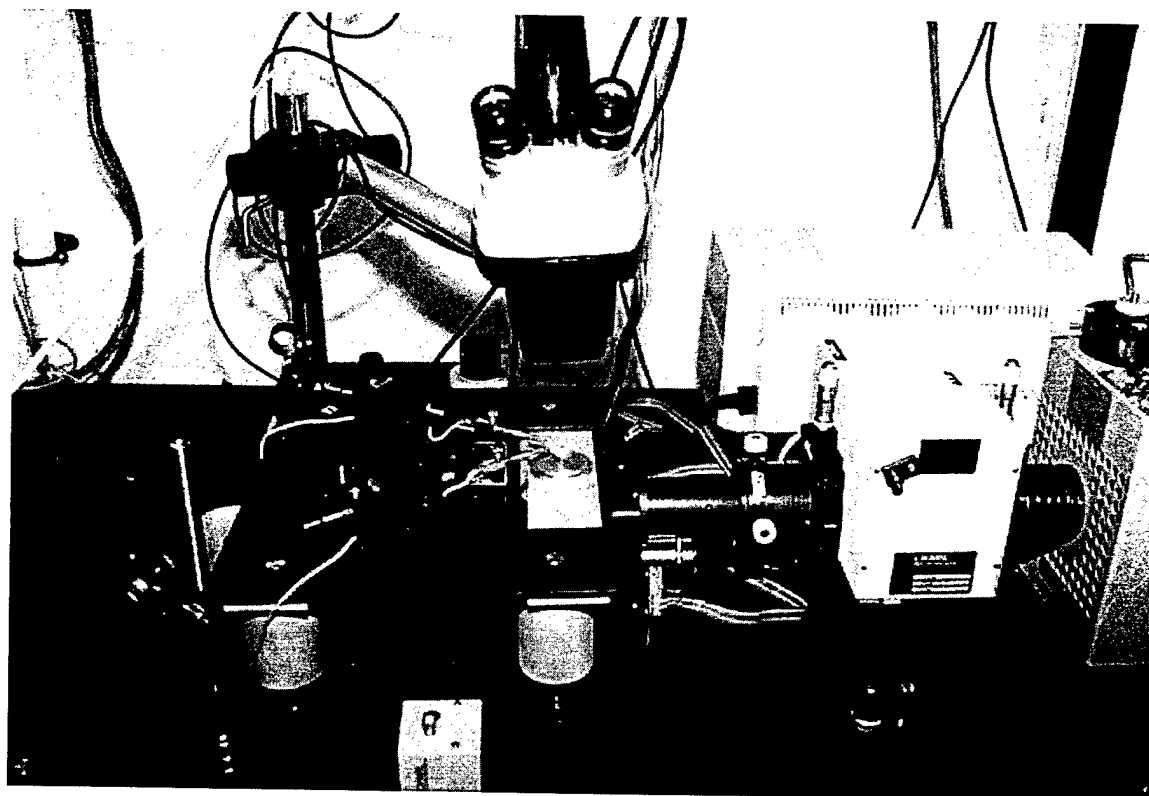


Figure 2.5 Experimental setup for measuring the spectral responsivity of the UV photodiode samples.

The 300K dynamic resistance of the photodiode at zero-bias  $R_0$  was also measured for selected devices using a shielded low-noise enclosure and shielded probe tips as shown in Figure 2.6. In these experiments, a Hewlett-Packard low-noise circuit analyzer was used to obtain the I-V characteristics of selected diodes in the dark enclosure under computer control from which the dynamic resistance  $R_0$  of the device at zero-bias was obtained. These measurements were combined with

the device area A to obtain the  $R_0A$  product. Equation 4 was then used to obtain an estimate of the detector detectivity  $D^*$ .

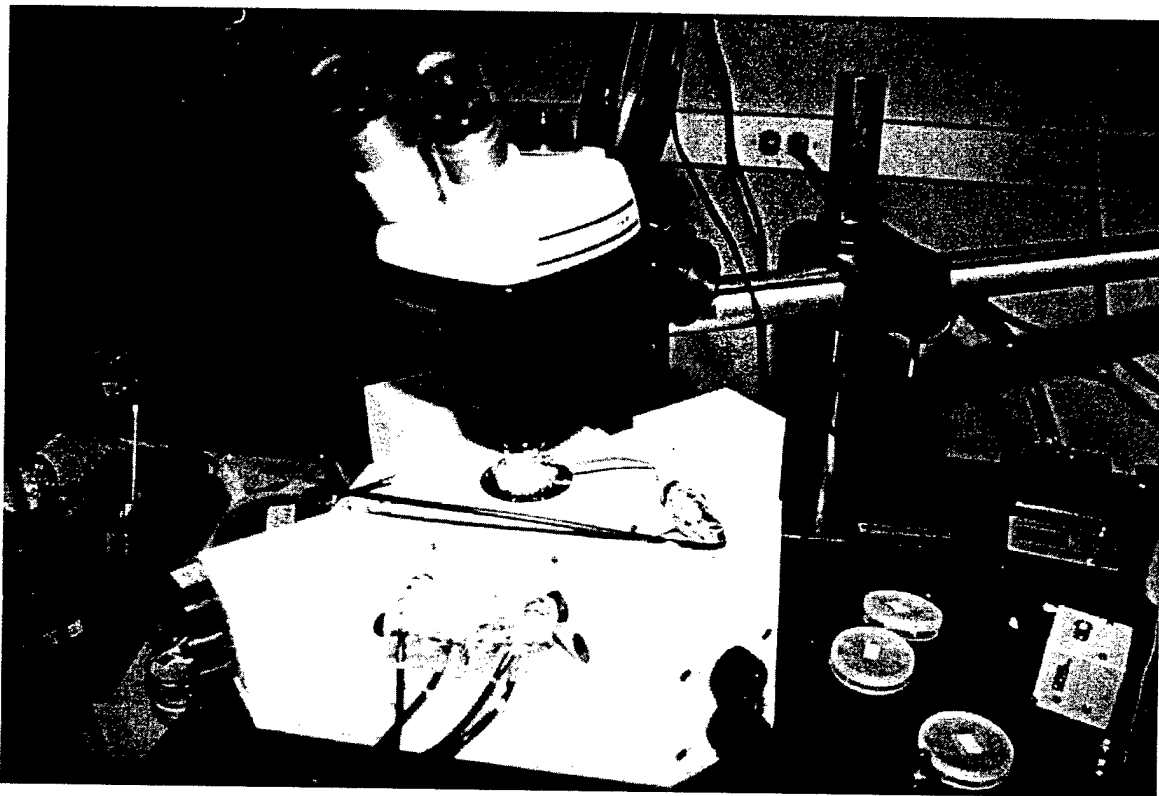


Figure 2.6 Equipment used to determine  $R_0A$  and  $D^*$  for selected photodiodes.

### 2.3.2 Photodiode Arrays

All of the photodiode array processing was completed at NCSU using standard semiconductor processing techniques which included photolithography using appropriately-designed masks, reactive ion etching to define mesa structures, and metallizations to provide ohmic contacts to the n-type and p-type layers of the device. The 128x128 photodiode array consists of 16,384 mesa diodes. The mesas are 32  $\mu\text{m}$  squares on a 38  $\mu\text{m}$  pitch, corresponding to a fill factor of 71%.

Photolithographically defined Ni was used to define the mesas, and  $\text{BCl}_3$  reactive ion etching was used to etch the mesas down to the n-type AlGaN base layer. Ni/Au and Ti/Al metallizations, followed by an anneal at 600 - 700 °C, were employed to obtain p-type and n-type ohmic contacts, respectively.

The 128x128 photodiode array was hybridized to a Indigo Systems silicon readout integrated circuit (ROIC) using indium bump bonds. In this procedure, photoresist was used to define 18  $\mu\text{m}$  circular vias at all of the p-contact and n-contact points of the photodiode array, and at the corresponding metal pads of the Si ROIC. A dedicated UHV deposition system, shown in Figure 2.7, which employs MBE-type effusion cells was then used to precisely deposit a uniform array of indium bumps of thickness 5.0  $\mu\text{m}$  onto both the photodiode array and the Si ROIC.

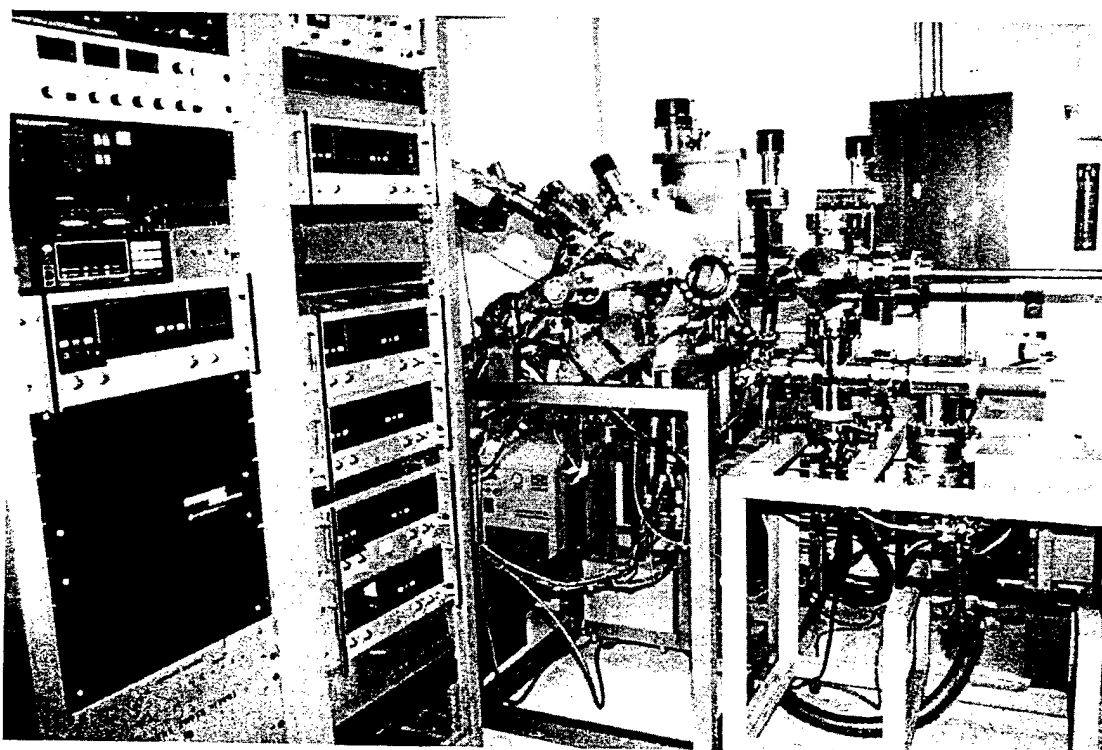
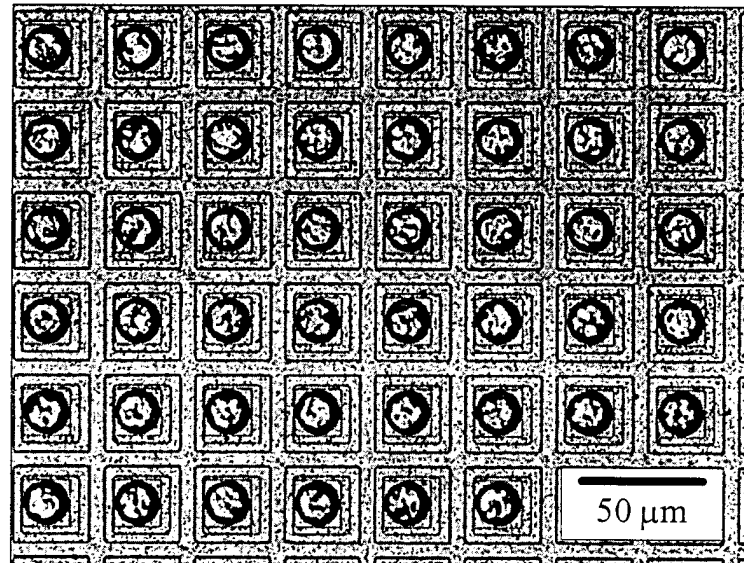
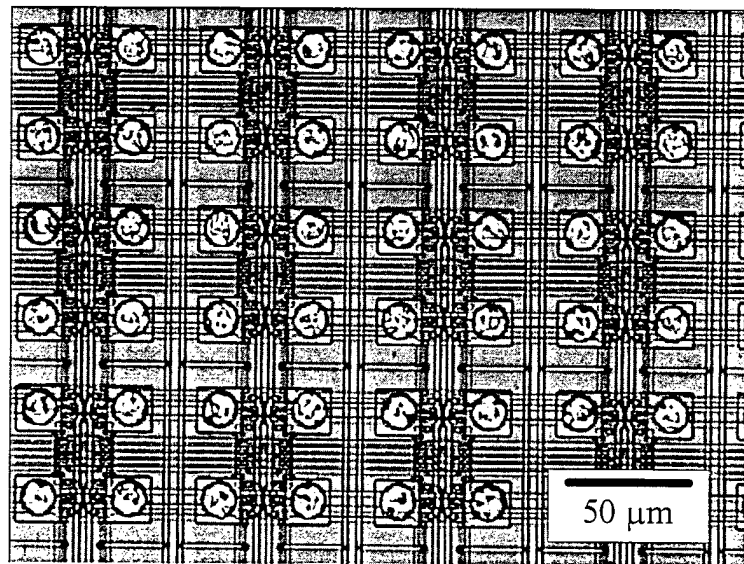


Figure 2.7 MBE chamber used for indium bump depositions.

Photographs of the 128x128 diode array and 128x128 silicon ROIC after the bump bonding procedure are shown in Figure 2.8 below.



**128x128 Photodiode Array**



**128x128 Silicon ROIC**

Figure 2.8 128x128 photodiode array and silicon ROIC after deposition of indium bumps.

The photodiode array was then hybridized to the Si ROIC using a RD Automation model M8-G flip-chip aligner bonder shown in Figure 2.9 below.

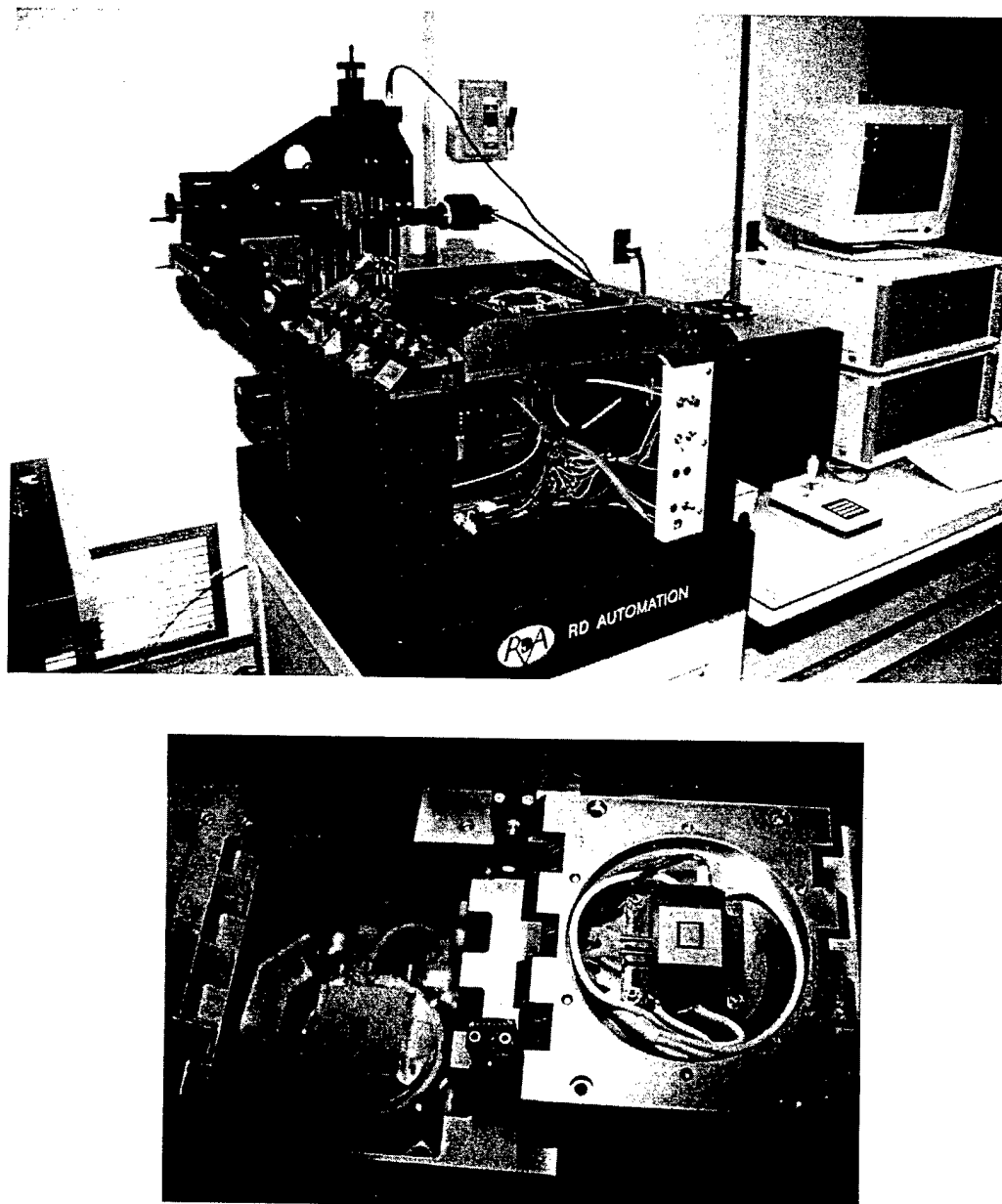


Figure 2.9 R D Automation M8-P flip chip bonder (top); platens holding diode array and ROIC onto vacuum chucks just prior to hybridization (bottom).

The 128x128 hybridized focal plane array (FPA) was then cemented onto an 84-pin leadless chip carrier (LCC). Outputs from the ROIC were then wire bonded to the LCC using gold wires as shown in Figure 2.10.

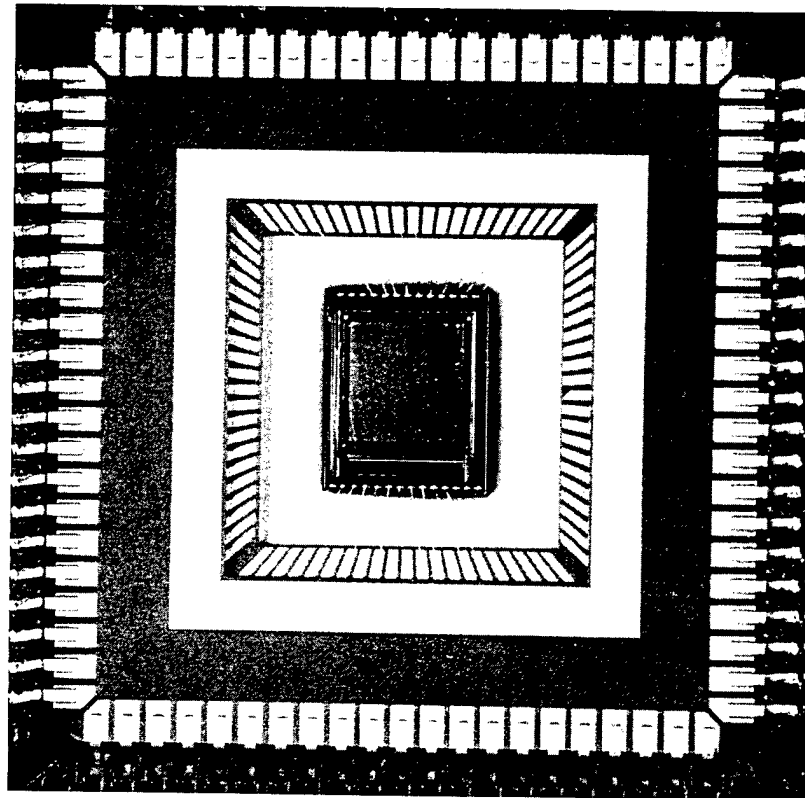


Figure 2.10 Hybridized 128x128 focal plane array imager mounted and wirebonded onto 84 pin leadless chip carrier.

Similar device processing steps, bump-bonding, hybridization and mounting procedures were employed to develop 320x256 focal plane array imagers. In this case, an Indigo Systems 9809 ROIC with a CTIA input circuit was employed. This chip is roughly 1000 times more sensitive than the Indigo Systems 9806 ROIC used for the 128x128 chip. A hybridized 320x256 UV focal plane array imager mounted onto a leadless chip carrier is shown in Figure 2.11

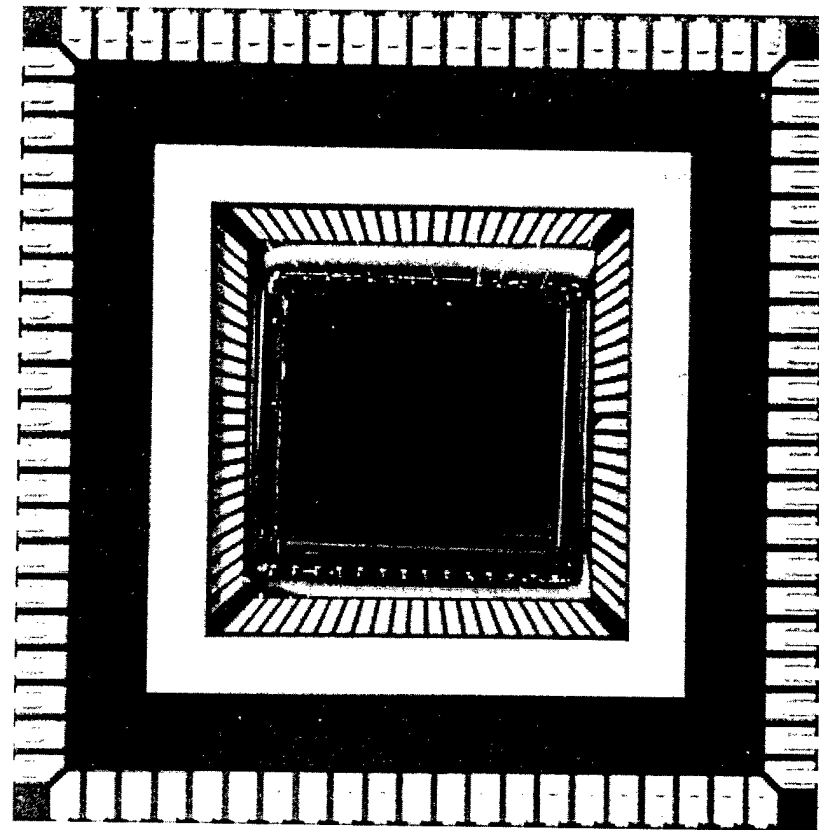
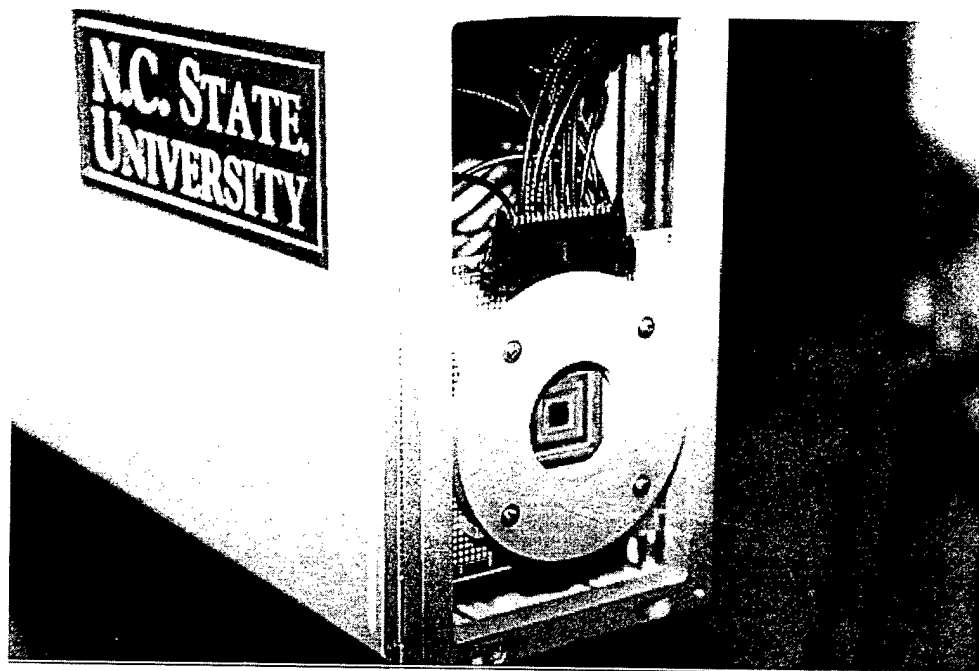


Figure 2.11 Hybridized 320x256 focal plane array imager mounted and wirebonded to 84 pin leadless chip carrier.

The selected UV camera chip was then inserted into a matching 84 pin socket located on a circuit board in the UV camera as shown in Figure 2.11. The UV camera, shown in Figure 2.12, employs a fused quartz focusing lens along with hardware and software for reading out, displaying, and storing UV images from the 128x128 and 320x256 FPAs at selected frame rates under computer control.

(a)



(b)

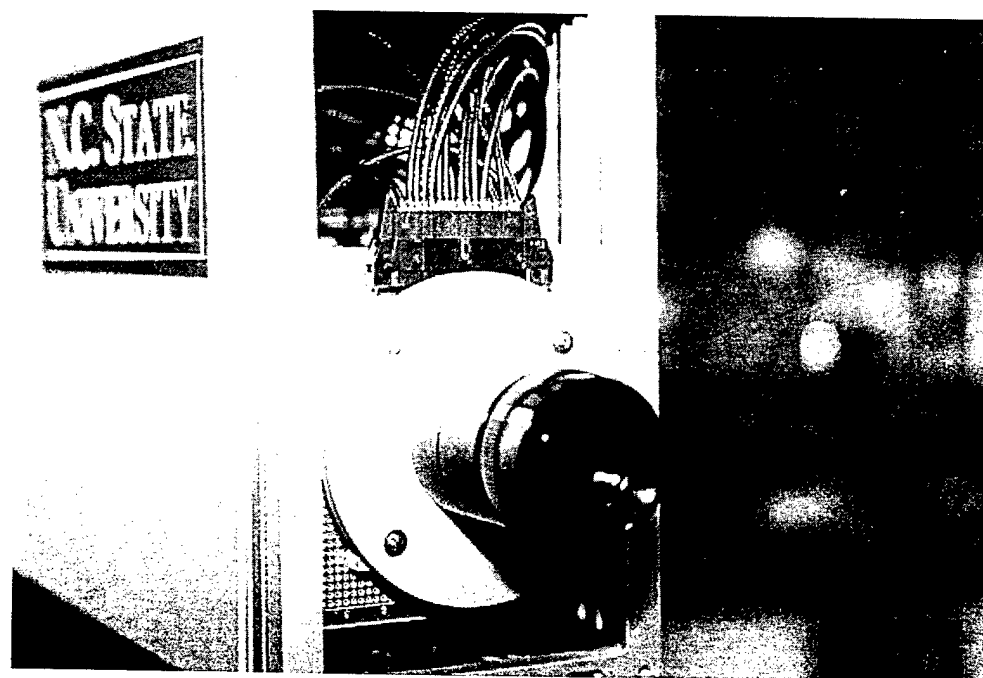
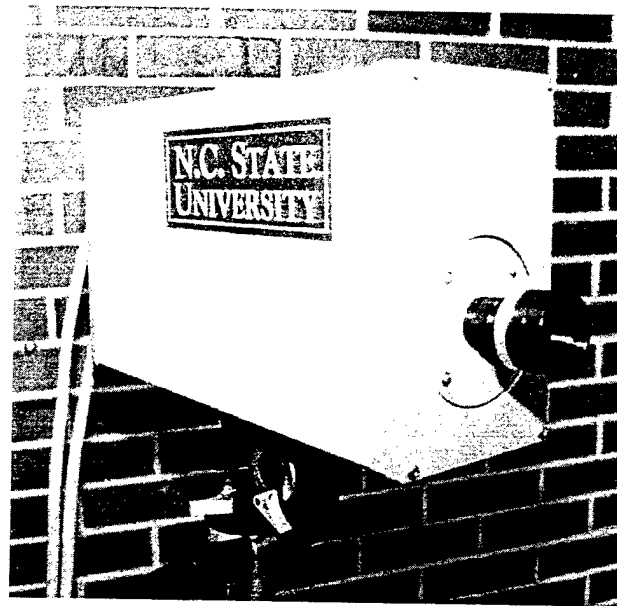


Figure 2.11 (a) UV FPA chip assembly mounted in LCC socket in UV camera head;  
(b) Camera head with quartz UV optics installed.

(a)



(b)

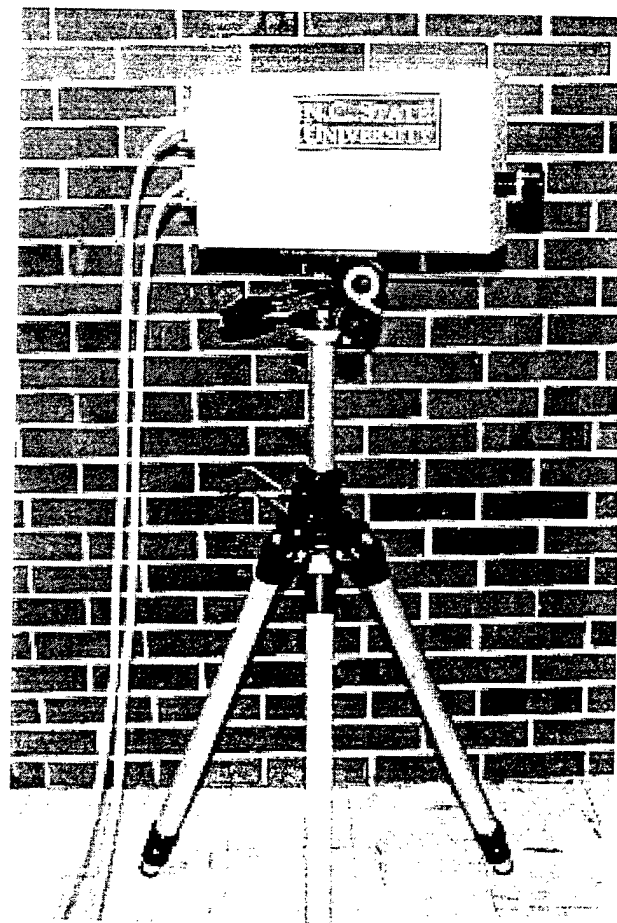


Figure 2.12 Two views of NCSU UV digital camera.

## 2.4 SE-IR Digital Camera and Focal Plane Evaluation Kit

### 2.4.1 Basic Operating Specifications

The SE-IR camera system shown in Figure 2.12 is used to test and demonstrate state of the art digital focal plane arrays (FPAs) designed for imaging IR, visible, or UV scenes. The standard system supports up to 800H x 600V single color arrays, 512H x 512V two color arrays and 320H x 256V four color FPA configurations. The system has a maximum pixel processing rate of 20 mega-pixels per second. This allows frame rates up to 300 Hz for a 256 x 256 FPA or up to 1K Hz for a 128 x 128 FPA. The system can be divided into three parts--the camera head, the digital electronics and the software

The camera head consists of a mounting board with leadless chip carrier socket, clock driver electronics, low noise bias supplies, analog signal conditioning electronics, A/Ds, an optional a multichannel DVM for monitoring bias voltages and currents and for measuring FPA and dewar temperatures and a linear analog power supply.

The camera head receives clocks through a parallel RS-422 port. Up to 24 clocks can be provided to the FPA though most FPAs require no more than 6. The clock drivers have adjustable rails. The minimum rail to rail voltage is 0.25V and the maximum swing is 20.0V. The clock voltage range is -10.0V to +10.0V. The clock slew rate is adjustable from 1ns/V to 16ns/V.

Four low noise bias supplies are available (expandable to 16) for providing FPA bias needs. They are used to provide power and any special voltages required by an FPA.

The signal conditioning electronics consist of pre-A/D analog electronics for controlling offset and gain before A/D conversion. Up to four output channels are supported in the standard configuration. The electronics support current output, voltage output and source/follower outputs requiring constant current supplies. The constant current supplies are adjustable from 200 uA to 3.5 mA for each channel. Signal offsets are added to the incoming signal to center the signal in the A/D range. Each channel can be independently adjusted for offset. The offset is software controlled. The range is +/- 10V in 4,096 steps. Each channel has independent gain control. There are three sets (low, medium and high) of four gains that can be used. The low, medium and high gain sets are selected by jumpers. The four gains in a set are software controlled. The combination of gain and offset control allow the output signals to be digitized with a maximized dynamic range. The A/Ds are 12 or 14 bits. There are 10 mega-samples per second with a noise floor between .6 and 1.0 LSB with a input referred noise less than 120 uV RMS. The aggregate sampling rate for all channels is limited to 20 mega-samples per second in the standard system. There are four special convert clocks available to control when sample conversion occurs. Each of these clocks can be delayed up to 1 msec in 2 nsec steps. This allows conversion of the output to occur at the optimum sampling point avoiding clock correlated noise spikes that may be present in the output channel while allowing for optimum settling. The A/D output are then multiplexed into a

single 16-bit wide video data stream. This data along with sync signals are sent over a high speed RS-422 interface to the digital electronics.

The standard interface cables to the clocks and digital video signals are 25 feet long and use SCSI-3 differential cables (the interface is NOT SCSI-3). Cables up to 150 feet can be used at full rate. Longer cables can be used at slower clock rates. This allows the camera head and digital electronics to be separated as may be required in some applications.

The digital electronics consist of three parts--a pattern generator board, a pipeline digital signal processor board, and a general purpose imaging processor board (Coreco F/64-DSP16).

The pattern generator board is a programmable timing generator with special features for operating FPAs. Patterns are defined as subpatterns. These subpatterns are output according to a control program. Up to three levels of looping are available along with synchronizing to external signals. The special features include the A/D conversion clocks mentioned earlier and the integration control clocks for controlling the integration time for a frame. There are up to four independent integration clocks that can be generated. Each integration clock can be duty cycle controlled and changed without stopping or reloading the timing patterns. The integration clocks can also be multiplexed together to allow super frames to be constructed consisting of two or four sequential frames with each frame having a different integration time. Sync signals are sent to the camera head and then returned to the digital signal processing electronics. This gives the sync signals the

same delays as the FPA clock and data signals so that they are independent of cable length.

The pattern generator uses a frequency generator so that precise clock rate control can be obtained. An external master clock can also be supplied to the pattern generator board. The pattern generator board is a full length, full height 16 bit ISA bus card.

The pipeline signal processor board is used to perform real-time pixel correction. The data is received through a high speed RS-422 parallel interface. The video and clock data is then fed into a set of pipeline processing. All operations in the pipeline are 16-bit to preserve data accuracy. Each operation is performed on a pixel by pixel basis. The first operation is a 2-point linear correction of each pixel to normalize response and offset (NUC, Non-Uniformity Correction). Separate coefficients are used for each pixel. The coefficient lists are 512K words (16-bits) long. The correction implemented is  $A*(X+B)$ . The user can perform image subtraction by including the image to be subtracted in the correction coefficient terms. After 2-point correction the pixel data is pipelined into pixel reordering hardware. This allows any pixel to be arbitrarily remapped to any other location in the image. This is used to perform bad pixel replacement by substituting a nearest good neighbor pixel. It also is used to mirror and/or rotate the image to correct for different optical configurations. The pixel reorder list is 512K words (18-bits) long.

The offset, gain and pixel reorder lists are synchronously downloaded so that no interruption in the image occurs and a frame is not updated in the middle. A list can be updated every other frame.

A single frame capture memory is used to capture a frame of data from the video stream after pixel reordering. This frame capture can also capture data during the sync periods. Some FPAs provide housekeeping data during this time. The capture memory can be accessed by the host computer without interrupting the processing stream. It can also be used by the host computer to perform equalization of the output image using the output lookup tables.

There are two 65K x 16-bit output lookup tables. These allow the user to perform various equalization or data clipping before the data is fed into the Coreco F/64-DSP16 general purpose image processor. Two LUTs are used so that one LUT can be updated while the other is processing data. The LUTs can then be switched by the hardware at the start of the next frame. The LUTs can be updated and switched every frame.

The output of the pipeline signal processor is the input to the Coreco F/64-DSP16 board. These boards are modified from the standard 12-bit digital interface to use a 16-bit digital interface. The Coreco F/64-DSP16 displays the live image on a monitor and performs user programmed image processing.

The CamIRa™ operating software includes SE-IR Corporation's CamIRa™ program and the CORECO Windows Development Toolkit. Source code, libraries and the CORECO Windows Development Toolkit are included for U.S. distribution

only. The software is used to setup, control and perform analysis on image data coming from the FPA. This includes 2-point correction, image subtraction, image statistics, FPA parameters setup (including frame rate and intergration time), image setup and orientation, image capture functions, display control and many other functions. The software operates under Windows 95/98 or Windows NT 4.0 SP3 or higher. Source and libraries are compatible with Microsoft Visual C/C++ V5.0 or higher.

#### **2.4.2 Procedure for Determining Diode Array Statistics**

In addition to providing UV digital images, the SE-IR camera system soft ware allows one to determine signal levels of each pixel of the digital array for a given frame readout. When the camera is illuminated, this maxtrix of signals corresponds to the information needed to read out and store the digital image. This procedure can then be used to generate a histogram of the the distribution of pixel signals that make up the digital image. If the digital focal plane array is placed in a light-free enclosure, the above procedure can be employed to obtain information about the noise characteristics of the array.

With the array in the dark, each pixel generates a "noise" voltage  $\Delta V$  on ROIC capacitor C for a given image integration time  $\Delta t$ , where  $\Delta V = \Delta q/C$  ( $\Delta q$  is the accumulated charge on the ROIC pixel capacitor, and C is the capacitance of the ROIC pixel capacitor). As a consequence, the dark noise current  $I_{ND}$  can be written as

$$I_{ND} = \Delta q/\Delta t = C\Delta V/\Delta t \quad (7)$$

where

$$C = 0.44 \mu V/e^- \text{ (128x128 ROIC)}$$

$$= 13.3 mV/e^- \text{ (320x256 ROIC)}$$

In terms of the dark noise current  $I_{ND}$ , the pixel NEP can be written as

$$NEP = I_{ND}/R_\lambda \quad (8)$$

where  $R_\lambda$  is the spectral responsivity of the pixel photodiode.

The spectral detectivity  $D^*$  for each pixel can also be obtained using

$$D^* = (A\Delta f)^{1/2}/NEP \quad (9)$$

where  $A$  is the area of the pixel photodiode and  $\Delta f$  is the bandwidth of the hybridized array. The SE-IR camera software can then produce histograms of the distribution of values for  $I_{ND}$ , NEP, and  $D^*$  for the entire hybridized array of pixels.

## 2.5 UV Imaging Techniques

The experimental setup that was used for testing the UV FPAs is shown in Figure 2.13. It consists of an alpha-numeric UV source, a quartz focusing lens, the UV digital camera, and a digital camera computerized imaging system. To illuminate solar-blind FPAs (250-285 nm) an Oriel model 6035 Hg(Ar) pencil lamp emitting monochromatic radiation at 253.6 nm was employed. For the visible blind arrays, the Oriel source was fitted with a 6042 fluorescent filter. This produced a UV output centered at about 350 nm with a FWHM of ~40 nm. In order to provide an alpha-numeric UV scene, a thin sheet of brass was used to mill out letters or geometric shapes. This brass template was then attached to the front of the UV source to provide a UV back-lighted scene. A number of additional template used in this work are shown in Figure 2.15. A fused quartz lens of focal length 25 mm was used to focus the UV scene onto the GaN/AlGaN FPA as shown in Figure 2.13.

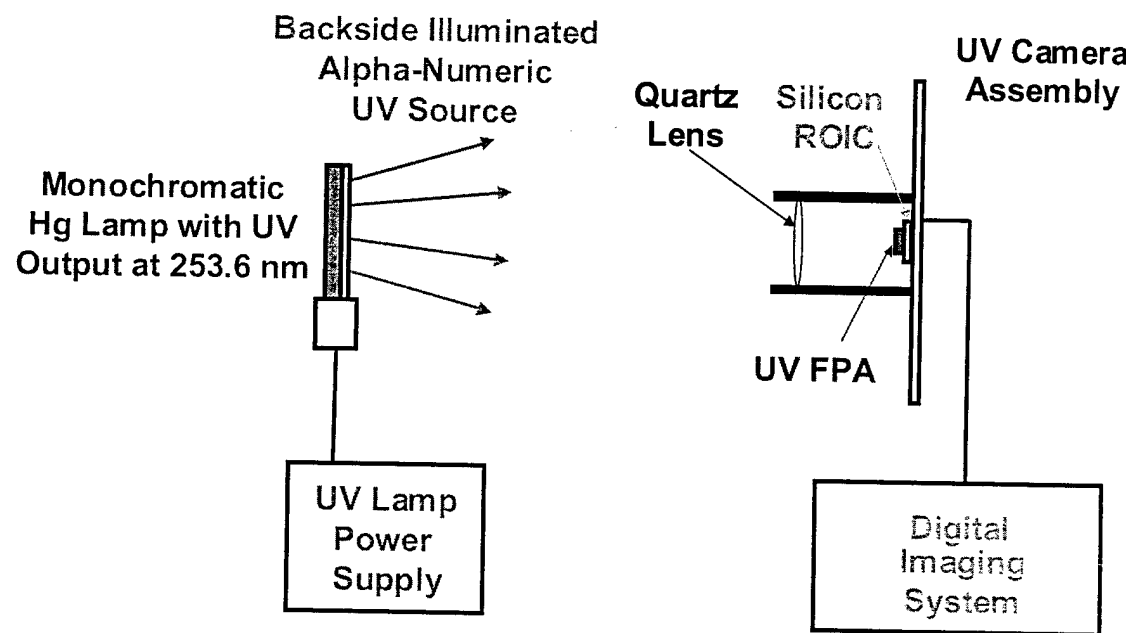


Figure 2.13 Experimental setup used to evaluate the solar-blind UV FPAs.

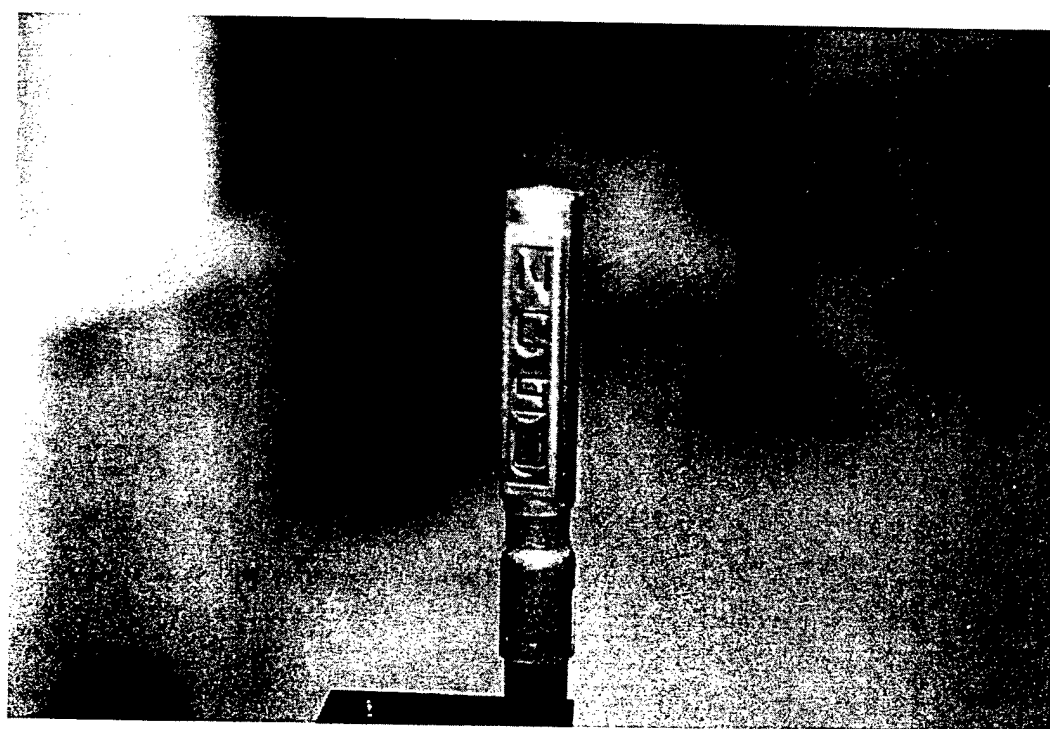


Figure 2.14 Back-lit UV alpha-numeric ("NCSU") source used for nitride FPA testing.

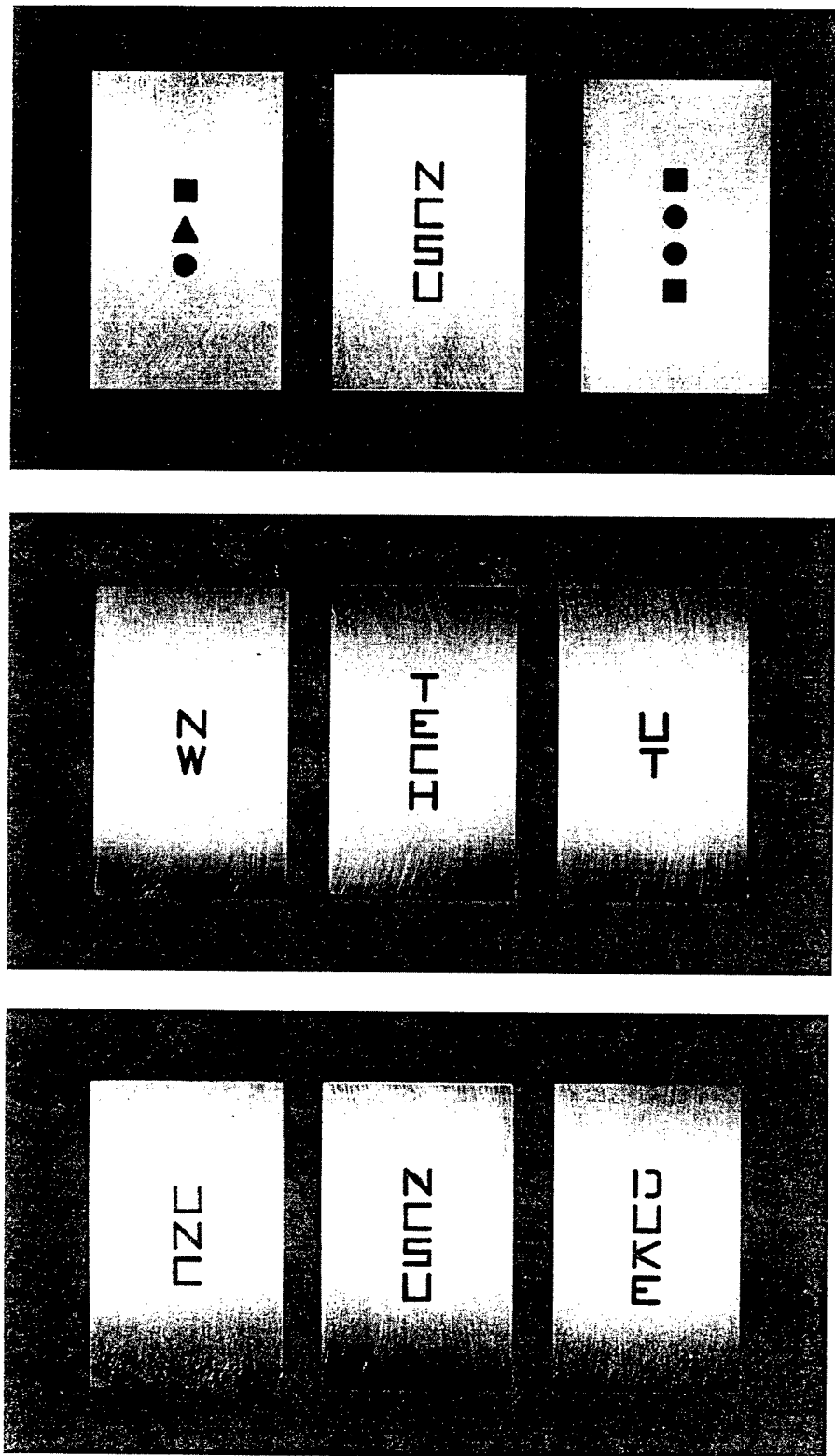


Figure 2.15 Additional templates used for UV imagery.

### 3. RESULTS AND DISCUSSION

#### 3.1 Characterization of Visible-Blind UV Photodiodes

The room temperature zero-bias spectral responsivity of a discrete GaN/AlGaN p-i-n heterostructure photodiode is shown in Figure 3.1. This particular device consists of a base n-type layer of  $\text{Al}_{0.2}\text{Ga}_{0.8}\text{N}$ , an undoped GaN layer, and a p-type GaN:Mg layer deposited by MOVPE. It is seen from the figure that the device has a sharp cut-on beginning at about 365 nm, which corresponds to the optical absorption edge of GaN at room temperature. The responsivity reaches its maximum value of 0.2 A/W at a wavelength of 358 nm. According to Equation 1, this corresponds to an external quantum efficiency of 70%. Assuming the reflection losses at the air-sapphire, sapphire-AlGaN, and AlGaN-GaN interfaces is about 12% [12], one obtains an internal quantum efficiency of about 82% for this device. The responsivity remains fairly constant until about 320 nm and then begins to decrease

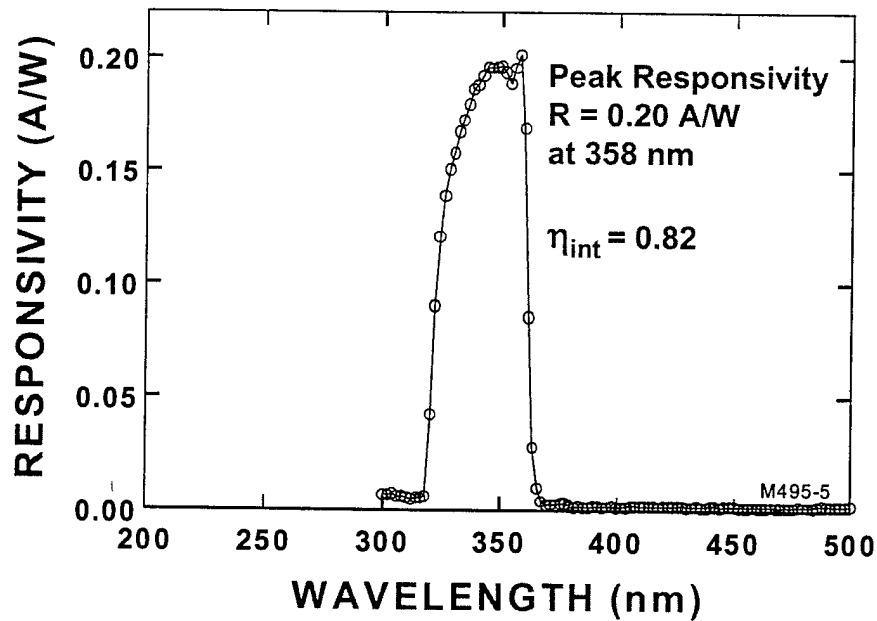


Figure 3.1 Responsivity of GaN/AlGaN heterostructure photodiode

rapidly as optical absorption occurs in the  $\text{Al}_{0.2}\text{Ga}_{0.8}\text{N}$  base layer of the device.

Figure 3.2 shows plots of the current-voltage (I-V) characteristics and the dynamic resistance  $dV/dI$  versus voltage for the discrete device. It is seen from the

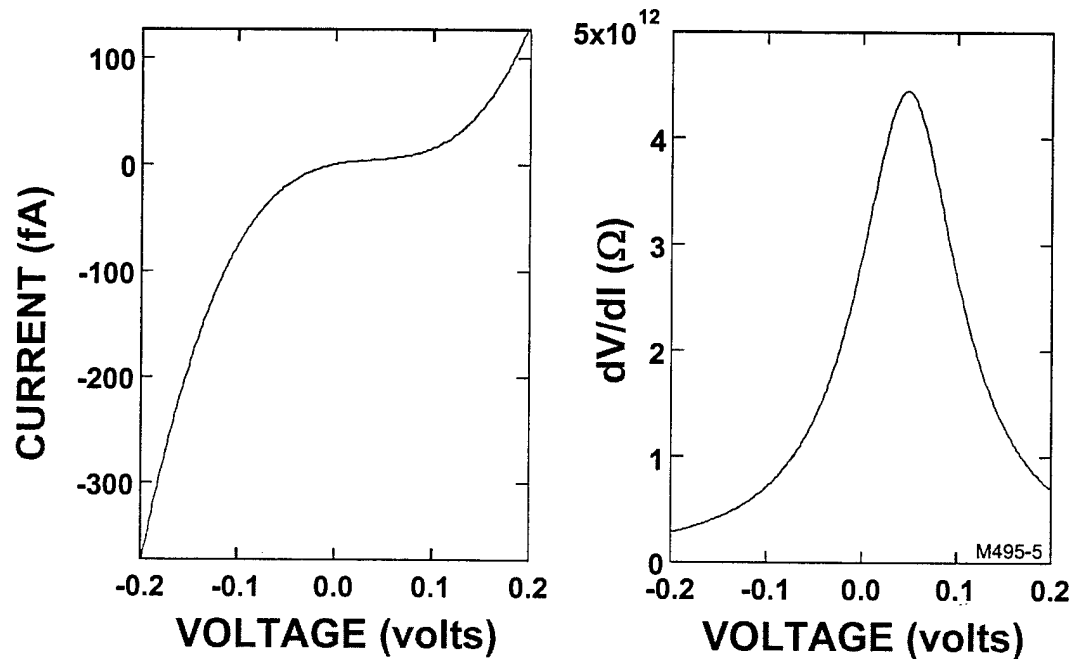


Figure 3.2 Current-voltage characteristics of a discrete  $\text{GaN}/\text{AlGaN}$  p-i-n heterostructure photodiode (left). The dynamic resistance versus voltage is also shown (right). Note that the diode dynamic resistance peaks near zero-bias and is very large. This implies high optical detectivity.  $R_0A = 1.5 \times 10^9 \text{ cm}^2$  and  $D^* = 6.1 \times 10^{13} \text{ cm Hz}^{1/2}\text{W}^{-1}$  were obtained for this device.

figure that the dynamic resistance peaks close to zero-bias, indicating that the device should be most sensitive to UV radiation when operated in the photovoltaic mode at or near zero-bias. Using the device area  $A$  along with Equation (3) one obtains  $R_0A = 1.5 \times 10^9 \Omega \text{ cm}^2$  and  $D^* = 6.1 \times 10^{13} \text{ cm Hz}^{1/2}\text{W}^{-1}$  for this discrete photodiode. This  $D^*$  value, obtained at room temperature, is one of the largest  $D^*$  values ever obtained for any semiconductor photodetector operating at any

temperature, as is illustrated by the  $D^*$  values for various devices shown in Figure 2.4. Note from the figure that the GaN/AlGaN p-i-n photodiode  $D^*$  value of  $6.1 \times 10^{13} \text{ cm Hz}^{1/2} \text{W}^{-1}$  is more than an order of magnitude higher than  $D^*$  values for UV-enhanced Si photodiodes at 358 nm, and is within a factor of five of  $D^*$  values associated with commercial UV-enhanced photomultiplier tubes at this wavelength.

Data for additional photodiode samples having peak responsivities in the 300-365 visible-blind UV region are shown below in Figure 3.3.

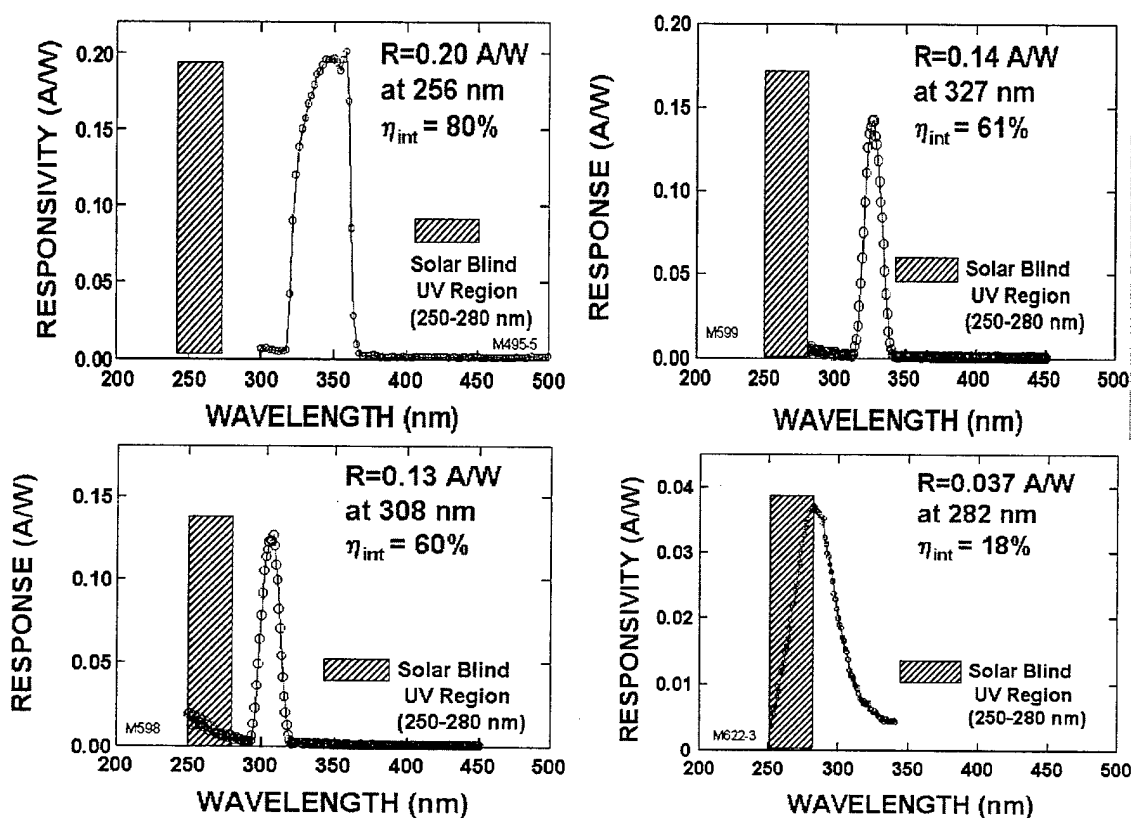


Figure 3.3 Responsivities for selected UV photodiodes in the visible-blind spectral region.

### 3.2 UV-Specific (320-365 nm) Digital Camera Based on 128x128 Focal Plane Arrays of GaN/AlGaN p-i-n Photodiodes

Digital images of a variety of UV scenes, obtained using 128x128 visible-blind FPA, are shown in Figures 3.4-3.9. Figure 3.4 shows a number of alpha numeric images obtained using the templates discussed in Section 2.5.

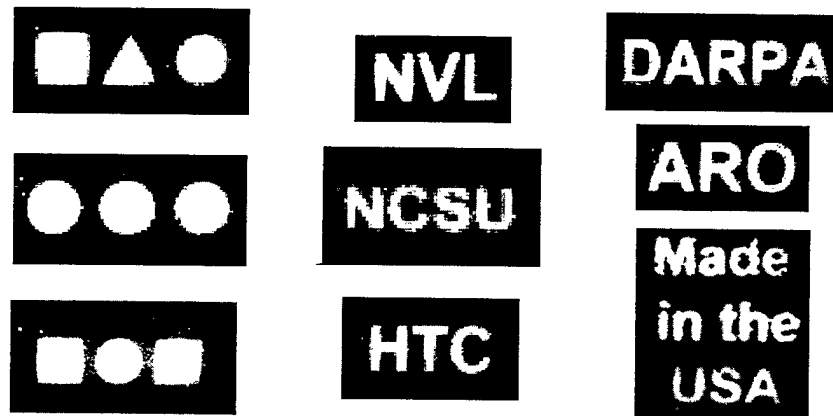


Figure 3.4 Visible-blind (320-365) images obtained using a 128x128 FPA.

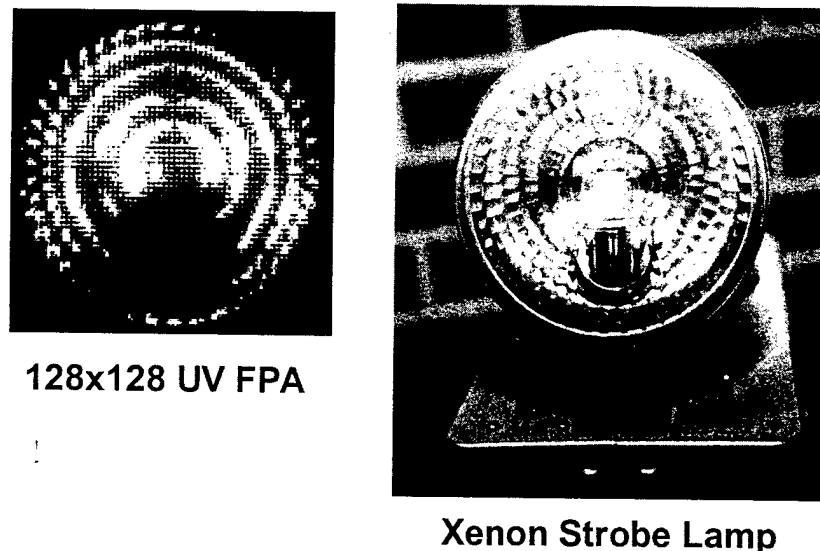


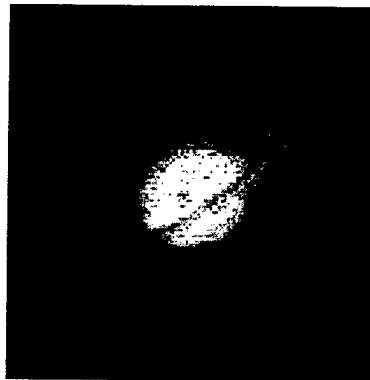
Figure 3.5 Visible-blind (320-365) image (left) of xenon strobe obtained using a 128x128 nitride UV FPA.



**Saturn**



**Mars**



**UV  
Images**

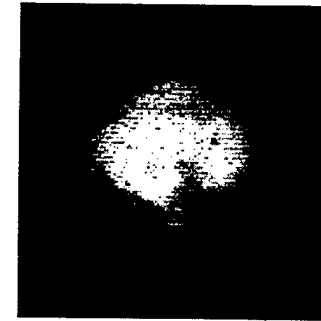
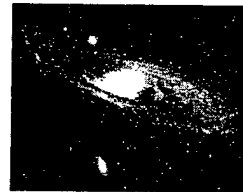
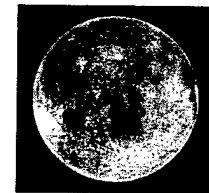


Figure 3.6 Visible-blind (320-365 nm) UV images of astronomical objects obtained using templates and a 128x128 UV FPA.



**Andromeda (M31)**

**Visible  
Images**



**Moon**



**UV  
Images**

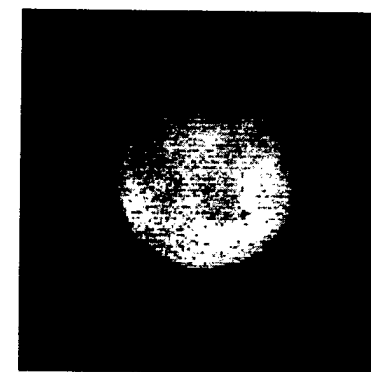
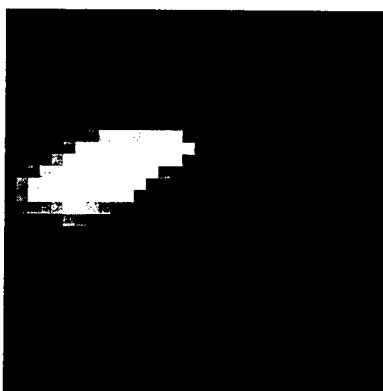


Figure 3.7 Visible-blind (320-365 nm) UV images of astronomical objects obtained using templates and a 128x128 UV FPA.

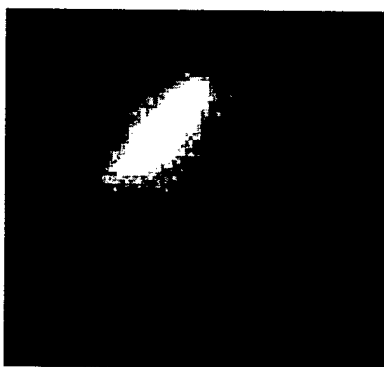
Figure 3.5 shows a UV image of a xenon strobe lamp obtained using a visible-blind UV FPA. It is seen from the figure that the array of back reflectors associate with the lamp are very well resolved in the UV image.

Figures 3.6 and 3.7 show UV images of astronomical objects obtained using templates in front of the filtered UV Hg-Ar source, as explained in Section 2.5. These images were obtained using a 128x128 visible-blind UV FPA (320-365 nm).

Visible-blind UV imagers operating in the 300-365 nm wavelength region are ideal for imaging a variety of hot sources such as flames and welding emissions. This application is illustrated in Figures 3.8 and 3.9 below. In Figure 3.6 is shown



32x32 FPA



128x128 FPA

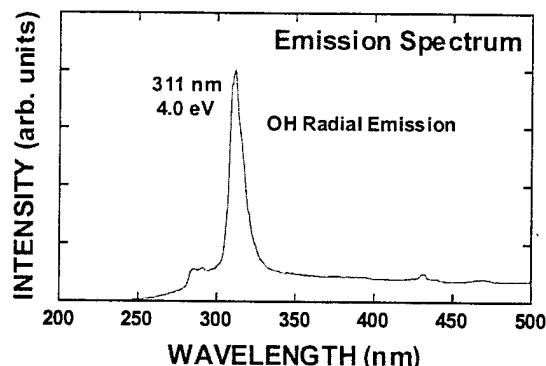


Figure 3.8 Visible-blind imagery of oxy-acetylene torch obtained using 32x32 and 128x128 UV FPAs. Note the improved resolution obtained using the 128x128 FPA.

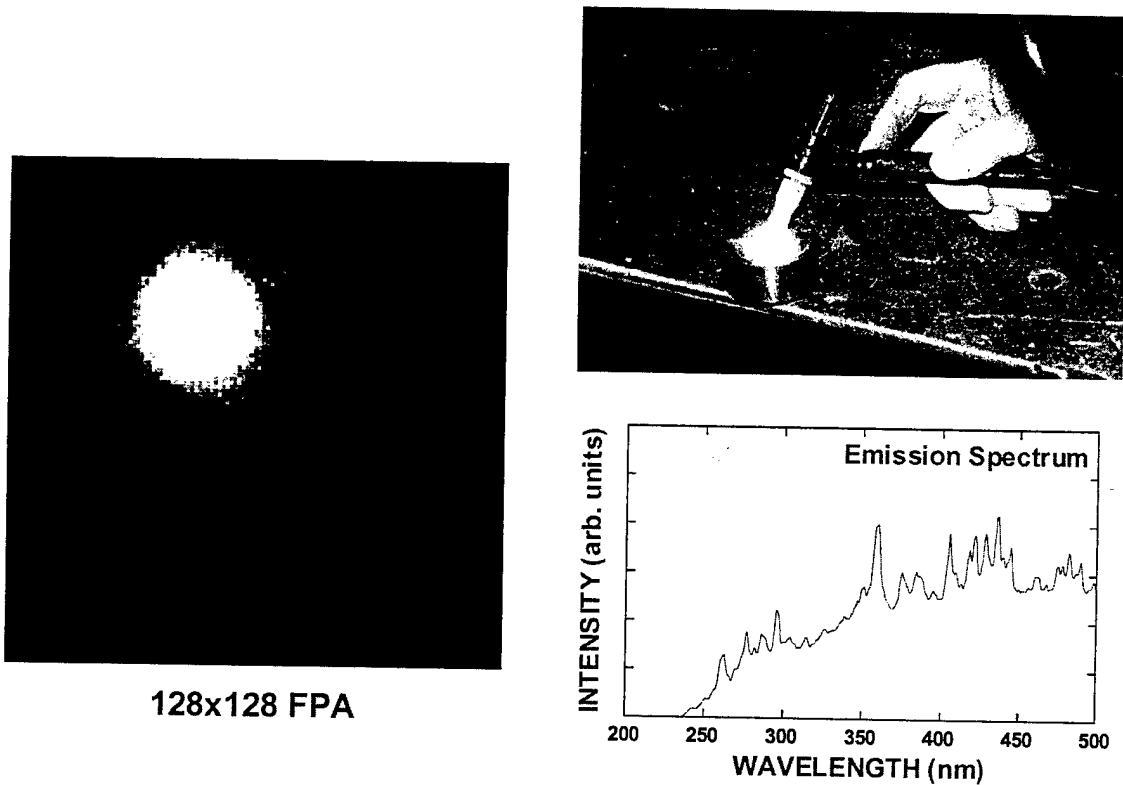


Figure 3.9 Visible-blind imagery of TIG arc welder obtained using 128x128 UV FPA.

### 3.3 Characterization of Solar-Blind AlGaN UV Photodiodes

The synthesis of truly solar-blind photodiodes requires MOVPE growth of high-Al content AlGaN alloys, as specified by Figure 2.2. During the materials development phase of the solar-blind detector electrical and optical characterization experiments were performed on the n-type and p-type layers of the device.

Figure 3.10 shows plots of optical absorption and cathodoluminescence for the base n-type AlGaN:Si layer (~64% Al) of the solar-blind photodiode structure. It is seen that the absorption edge is quite steep with little or no below-bandgap absorption.

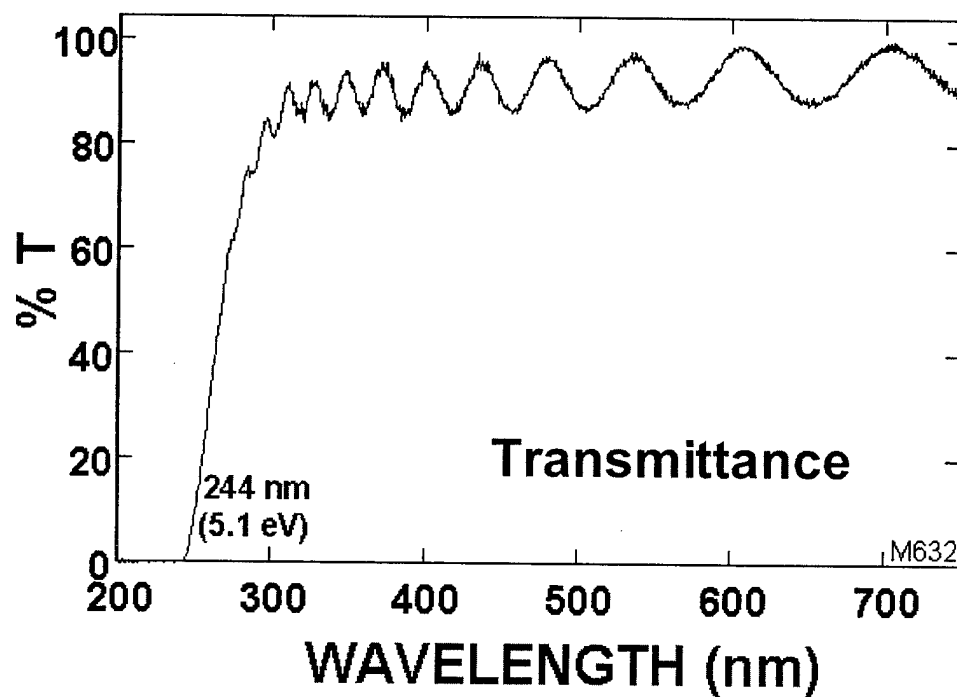


Figure 3.10 Optical transmittance and cathodoluminescence for n-type AlGaN:Si that forms the base layer of the solar blind detector structure.

The cathodoluminescence for this sample is dominated by near-bandedge emission at 247 nm. The spectrum also contains a broad peak centered at about 440 nm that is thought to be associated with the Si doping process. (This blue-violet emission is similar to the yellow-green emission that occurs in n-type GaN:Si but is shifted to shorter wavelength in the larger bandgap AlGaN sample).

Capacitance-voltage (C-V) measurements at low (1 KHz) and high (1 MHz) frequencies were performed in order to estimate the net donor density  $N_d - N_a$  and the free carrier density, respectively [12,13]. The low frequency capacitance should be dependent on the density of deep and shallow impurities  $N_d - N_a$ , while the high frequency capacitance depends on the free carrier density  $n$  [13]. From such measurements on the optimized  $\text{Al}_{0.64}\text{Ga}_{0.36}\text{N:Si}$  base layer of Figure 3.10 one obtains  $N_d - N_a \sim 1.0 \times 10^{18} \text{ cm}^{-3}$  and  $n \sim 3.0 \times 10^{17} \text{ cm}^{-3}$ .

Low and high frequency C-V measurements on n-type GaN:Si samples generally give the same numerical result for  $N_d - N_a$  and  $n$ , implying that the silicon donors are completely ionized at 300K. For the  $\text{Al}_{0.64}\text{Ga}_{0.36}\text{N:Si}$  sample, however, the C-V results suggest that only about 30% of the Si donors are ionized at 300K. If one assumes that the unintentional acceptor density  $N_a$  is negligible, one can estimate the ionization energy  $E_d$  of the Si donor for this AlGaN alloy samples from the C-V results since

$$n = N_d \exp(-E_d/2kT) \quad (10)$$

Using  $N_d = 1.0 \times 10^{18} \text{ cm}^{-3}$  and  $n = 3.0 \times 10^{17} \text{ cm}^{-3}$  in Equation 10 yields

$$E_d \sim 60 \text{ meV.} \quad (11)$$

for the  $\text{Al}_{0.64}\text{Ga}_{0.36}\text{N}:S$  alloy. This result is plotted in Figure 3.11 for AlGaN alloys having different Al content up to 64%.

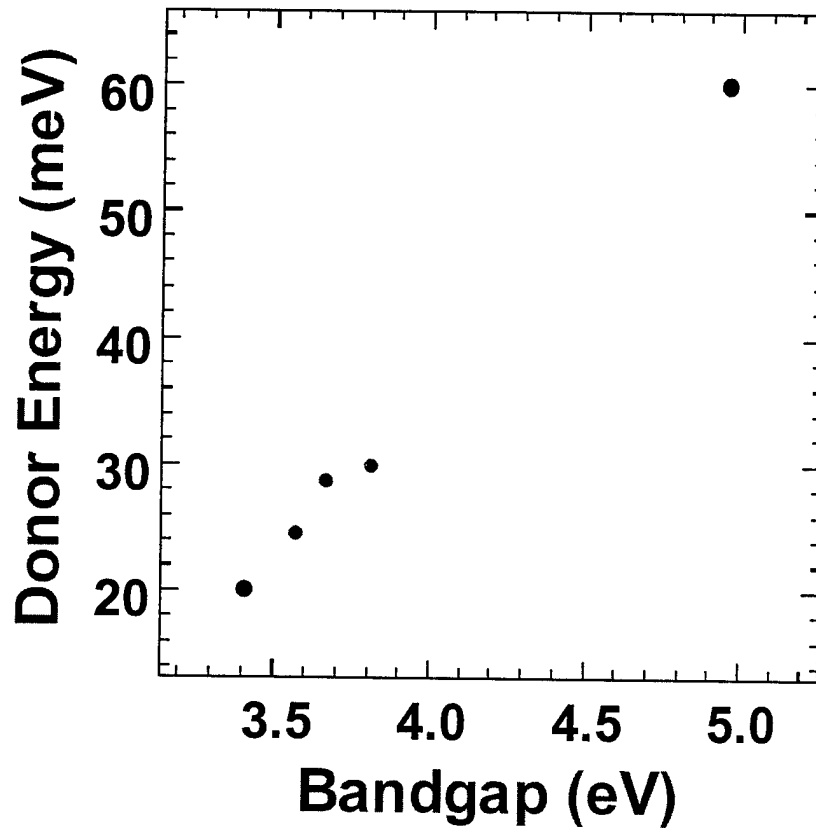


Figure 3.11 Estimate of the Si donor ionization energy for AlGaN alloy having bandgaps from 3.41 eV (GaN) up to 4.96 eV ( $\text{Al}_{0.64}\text{Ga}_{0.36}\text{N}$ ).

Figure 3.12 shows plots of optical absorption and cathodoluminescence for the top p-type AlGaN:Mg layer (~45% Al) of the solar-blind photodiode structure. It is seen that the absorption edge for this p-type layer is again quite steep with little or no below-bandgap absorption, except for a slight absorption in the 290-320 nm wavelength region. The cathodoluminescence is dominated by a large peak centered at about 350 nm. This UV peak is associated with the p-type doping process and grows in magnitude as the Mg dopant is increased during film growth.

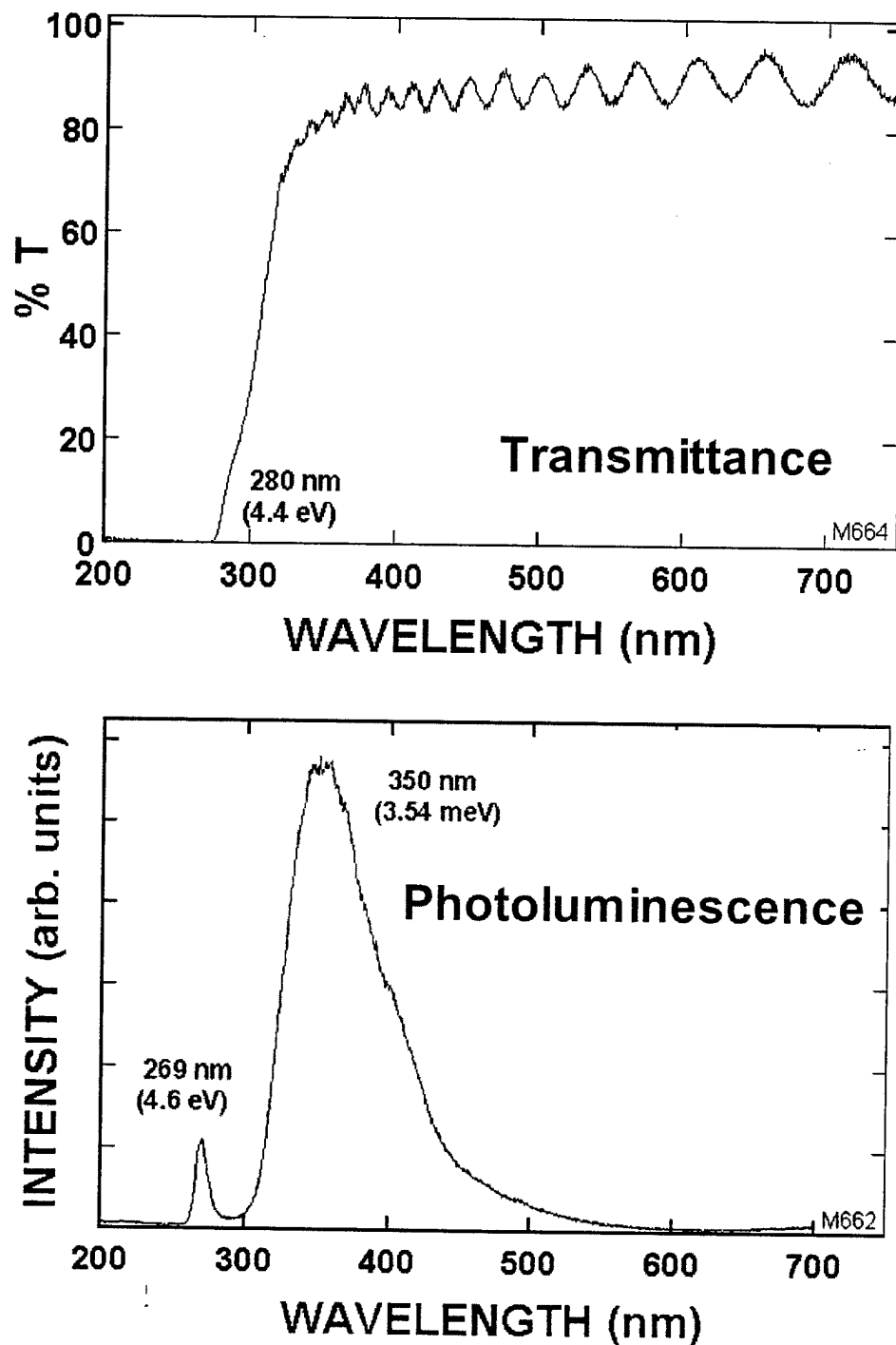


Figure 3.12 Optical transmittance and cathodoluminescence for p-type AlGaN:Mg layer (45% Al) that forms the top layer of the solar blind detector structure. The layer was subjected to a thermal anneal at  $700^{\circ}\text{C}$  to activate the dopant.

The observed deep level peak at ~350 nm is similar to the broad blue emission at about 440 nm that is observed for Mg-doped and annealed p-type GaN:Mg grown by MOVPE. We interpret this as evidence that p-type doping has been achieved for  $\text{Al}_{0.45}\text{Ga}_{0.55}\text{N}$  doped with Mg.

C-V measurements on the AlGaN:Mg layers were difficult to interpret due to low concentrations of holes. However, we have used such measurements to estimate the hole concentration in  $\text{Al}_{0.45}\text{Ga}_{0.55}\text{N}:\text{Mg}$  to be about  $5 \times 10^{15} \text{ cm}^{-3}$  for an acceptor concentration of  $2 \times 10^{19} \text{ cm}^{-3}$ . With these values, using

$$p = N_a \exp(-E_a/2kT) \quad (12)$$

one obtains an estimate of the Mg acceptor ionization energy. Solving (12) for  $E_a$  yields

$$E_a \sim 410 \text{ meV} \quad (13)$$

For  $\text{Al}_{0.45}\text{Ga}_{0.55}\text{N}:\text{Mg}$ . This result is plotted in Figure 3.13 below. These data indicate that the Mg acceptor is a very large in AlGaN, and increases with Al content. However, this work is very preliminary and needs to be checked with many additional experiments.

Figure 3.14-3.17 show the spectral responsivities obtained for representative solar-blind heterostructure photodiodes at zero bias (photovoltaic mode). The solar-blind devices exhibits a very narrow UV spectral responsivity band peaked at 267-273 nm, well within the 240 - 285 nm solar blind window, with a FWHM ~ 20 nm. The maximum responsivity  $R = 0.084 \text{ A/W}$  at 267 nm corresponds to an internal quantum efficiency of 42%. The responsivity falls off sharply at wavelengths greater

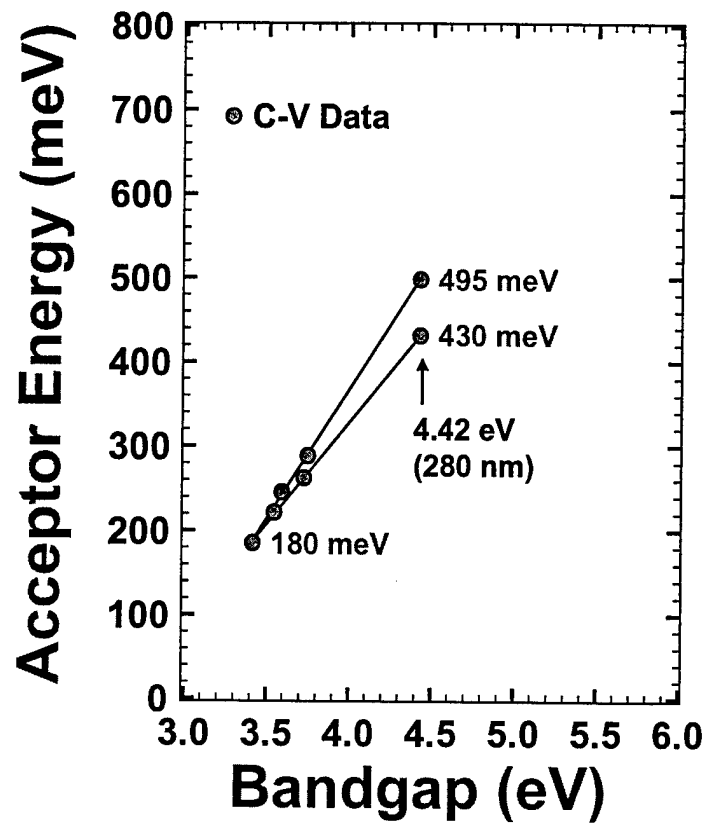


Figure 3.13 Estimate of the Mg acceptor ionization energy for AlGaN alloy having bandgaps from 3.41 eV (GaN) up to 4.42 eV ( $\text{Al}_{0.45}\text{Ga}_{0.55}\text{N}$ ).

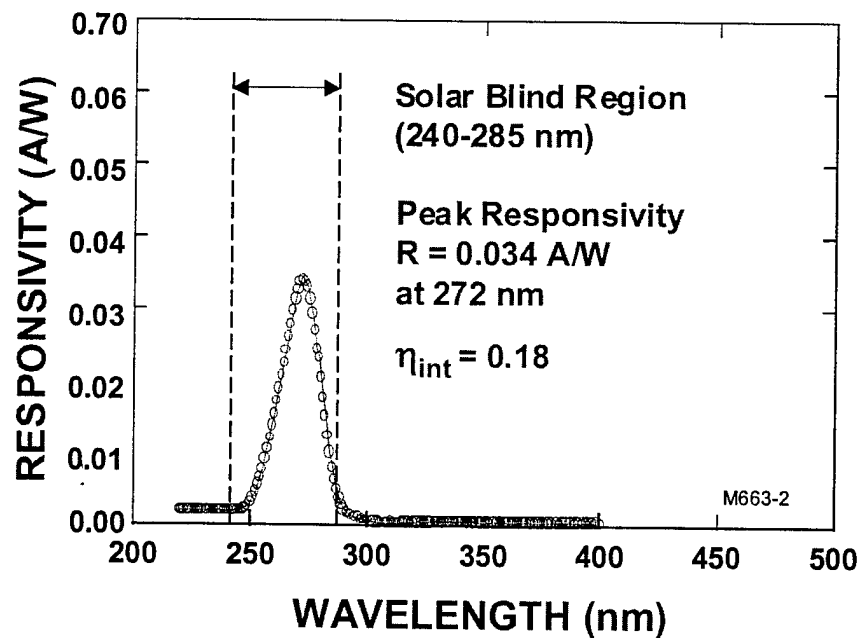


Figure 3.14 Responsivity of solar-blind AlGaN photodiode.

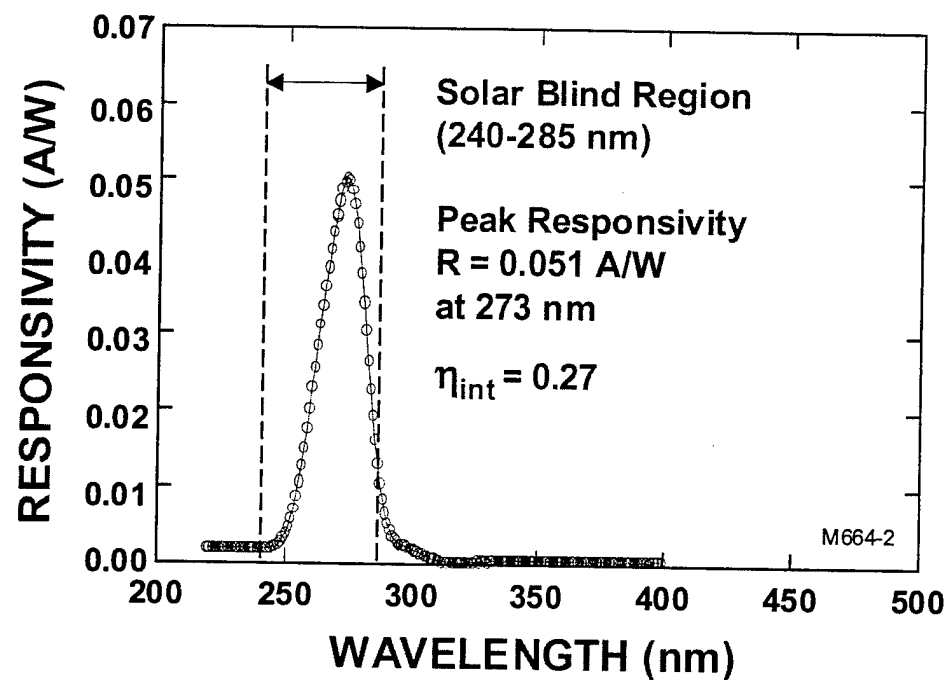


Figure 3.15 Responsivity of solar-blind AlGaN photodiode.

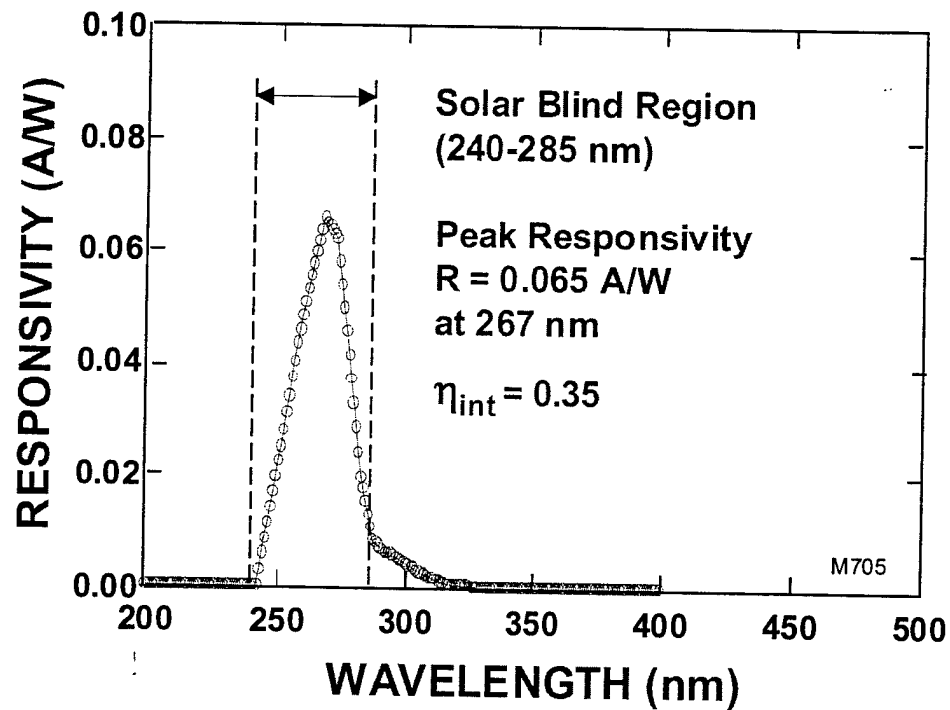


Figure 3.16 Responsivity of solar-blind AlGaN photodiode.

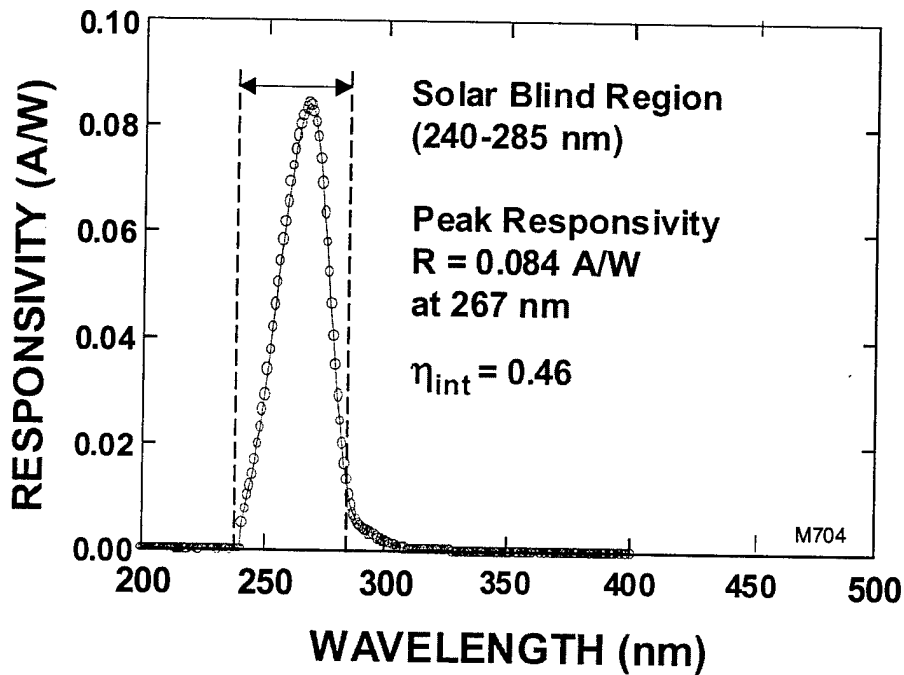


Figure 3.17 Responsivity of solar-blind AlGaN photodiode.

than 285 nm since the devices are transparent in this wavelength region. Likewise, the responsivities becomes very small at wavelengths shorter than 240 nm due to absorption in the n-type  $\text{Al}_{0.64}\text{Ga}_{0.36}\text{N:Si}$  base layer of the device. Thus, the AlGaN heterostructures that have been developed produced a narrow solar-blind responsivity band without the need for any external filters.

Figure 3.18 shows plots of the current-voltage ( $I$  vs  $V$ ) and the dynamic resistance  $DV/DI$  vs  $V$  exhibited by the solar-blind photodiode structure of Figure 3.17. As seen from the figure, the dynamic resistance of this  $200 \mu\text{m} \times 200 \mu\text{m}$  square mesa device peaks at about  $2 \times 10^{11} \Omega$  at zero bias, corresponding to  $R_0A =$

$8 \times 10^7 \Omega\text{-cm}^2$ . Substituting this value for  $R_0A$  along with the measured responsivity  $R_\lambda$  into (4) yields a detectivity  $D^* = 5.2 \times 10^{12} \text{ cmHz}^{1/2}\text{W}^{-1}$  at 267 nm.

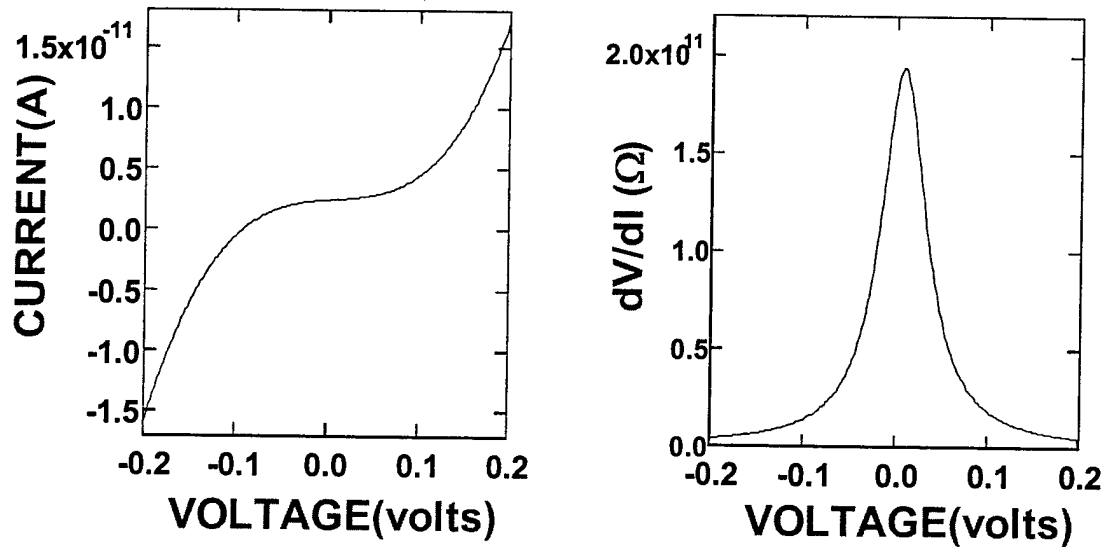


Figure 3.18 Electrical characteristics of solar-blind AlGaN heterostructure photodiode.

Figure 3.19 shows plots of  $D^*$  versus wavelength for a large selection of photodetectors. It is seen from this figure that the  $D^*$  value of  $3.3 \times 10^{12} \text{ cmHz}^{1/2}\text{W}^{-1}$  reported here for the AlGaN solar-blind heterostructure photodiode is somewhat smaller than  $D^*$  values that we have reported earlier for visible-blind nitride photodiodes which ranged up to  $D^* = 6.3 \times 10^{13} \text{ cmHz}^{1/2}\text{W}^{-1}$ . Note however, that these initial solar-blind AlGaN photodiodes exhibit a  $D^*$  value comparable to that of a UV-enhanced Si photodiode. However, a Si photodiode responds to radiation out to 1.1  $\mu\text{m}$  -- the fundamental absorption edge of Si. For a Si photodiode to respond only to radiation within the 240-285 nm solar-blind UV window, special external filters must be employed. Unfortunately, this filtering process reduces the Si solar-

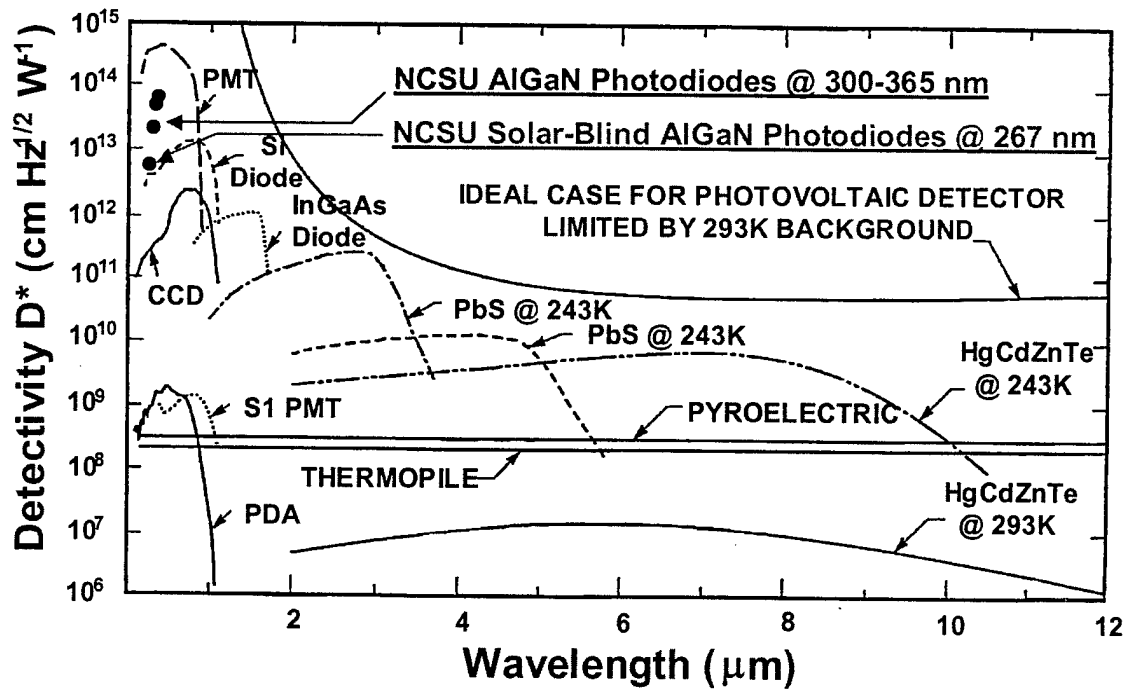


Figure 3.19 Detectivity versus wavelength for selected photodetectors.

blind responsivity by nearly two orders of magnitude to about  $D^* = 4 \times 10^{10}$   $\text{cmHz}^{1/2}\text{W}^{-1}$ . Thus, for solar-blind applications, the initial AlGaN heterostructure photodiodes reported herein are considerably more sensitive than comparable Si devices.

### 3.4 Properties of 128x128 and 320x256 Solar-Blind Focal Plane Arrays of AlGaN UV Photodiodes

Digital images of a variety of UV scenes, obtained using 128x128 solar-blind FPA, are shown in Figures 3.20-3.21. These images were obtained using templates that were back-illuminated with a monochromatic Hg(Ar) source (output at 253.6 nm). Digital movies at 60 hz were also obtained, but these cannot be shown as part of this final report.

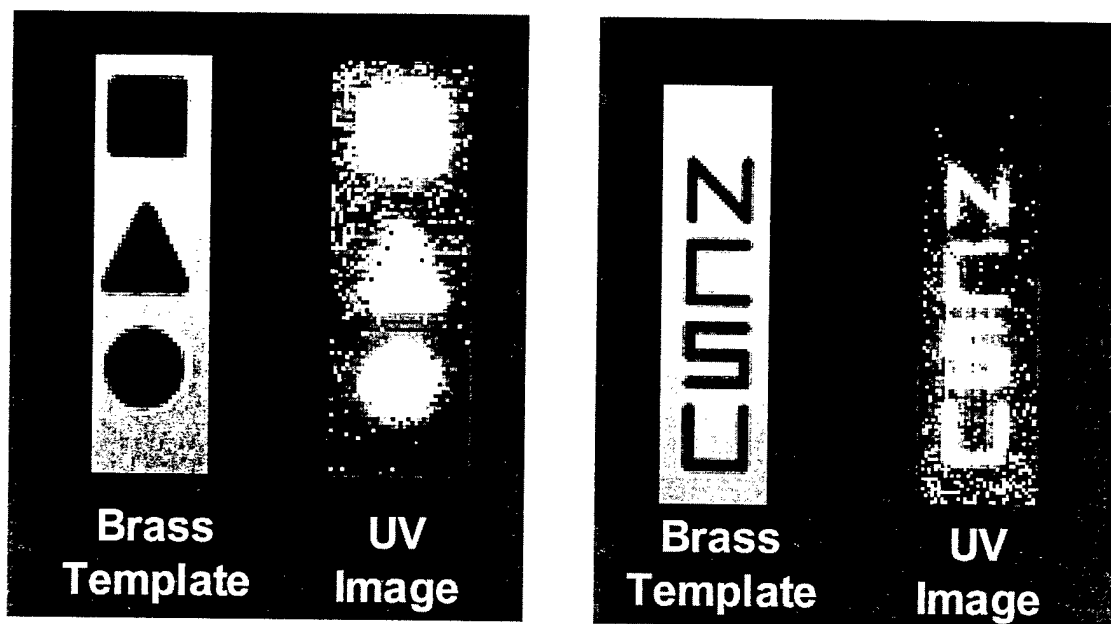


Figure 3.20 Digital images obtained using 128x128 solar-blind UV FPAs.

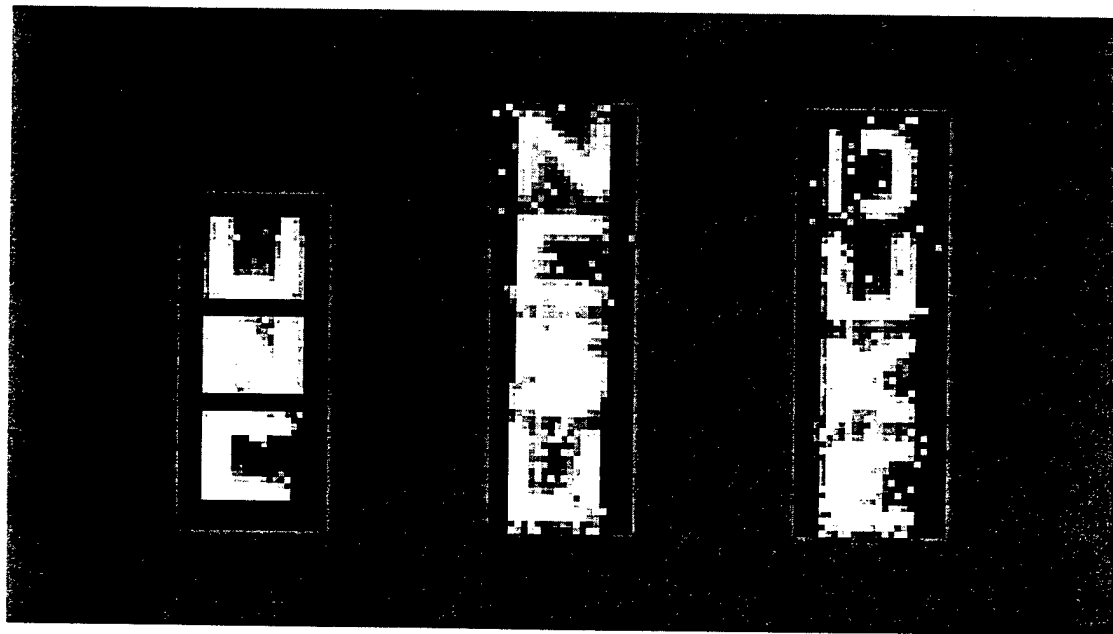


Figure 3.21 Digital images obtained using 128x128 solar-blind UV FPAs.

Additional solar-blind UV images were obtained using a 320x256 diode array hybridized to an Indigo Systems 9809 ROIC having more sensitive CTIA input circuitry. Several of these solar-blind UV digital images are shown in Figures 3.22 and 3.23 below. In addition to single-frame images, a number of digital movies

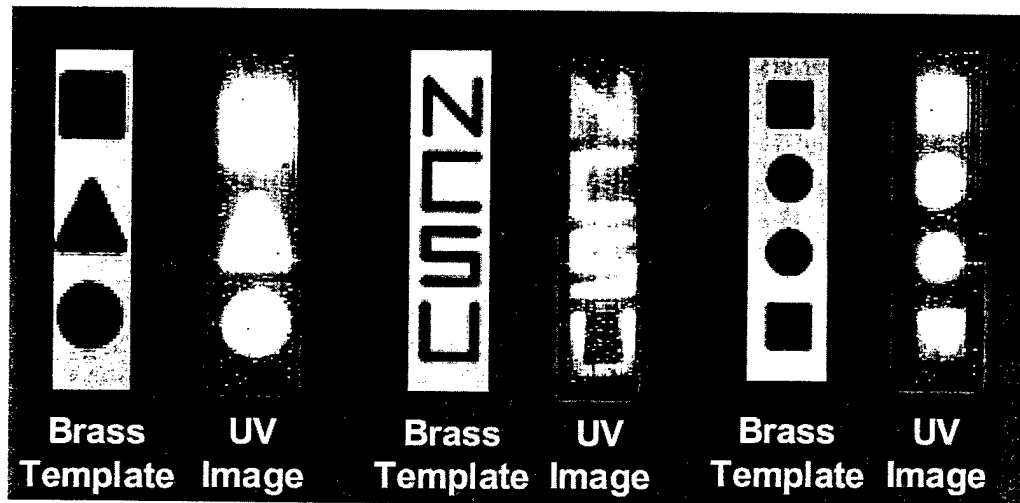


Figure 3.22 Solar-blind UV images obtained using a 320x256 AlGaN FPA.



Figure 3.23 Solar-blind UV images obtained using a 320x256 AlGaN FPA.

were obtained, but these cannot be included in this report document.

### 3.5 Diode Array Statistics

Using the techniques described in Section 2.4.2 of this final report, diode array statistics were obtained for both visible-blind and solar-blind FPAs. These results are shown in Figures 3.24-3.27. In Figure 3.24 the dark current and NEP for the 128x128 9806 ROIC (direct injection) and the 320x256 9809 ROIC (CTIA injection) are shown. In this case, the distributions correspond to the noise generated in the ROICs, since no diode arrays were attached via bump-bonding. It is seen from

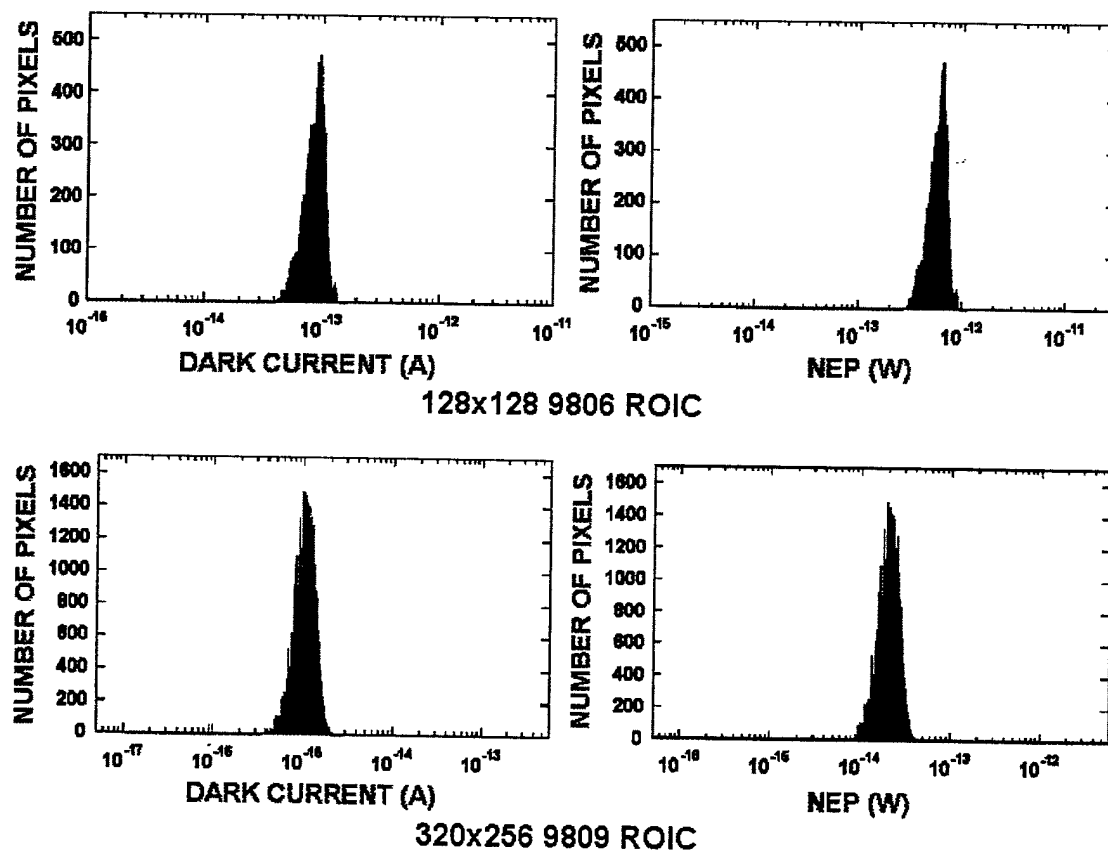


Figure 3.24 Dark current and NEP statistics for 9806 and 9809 ROICs.

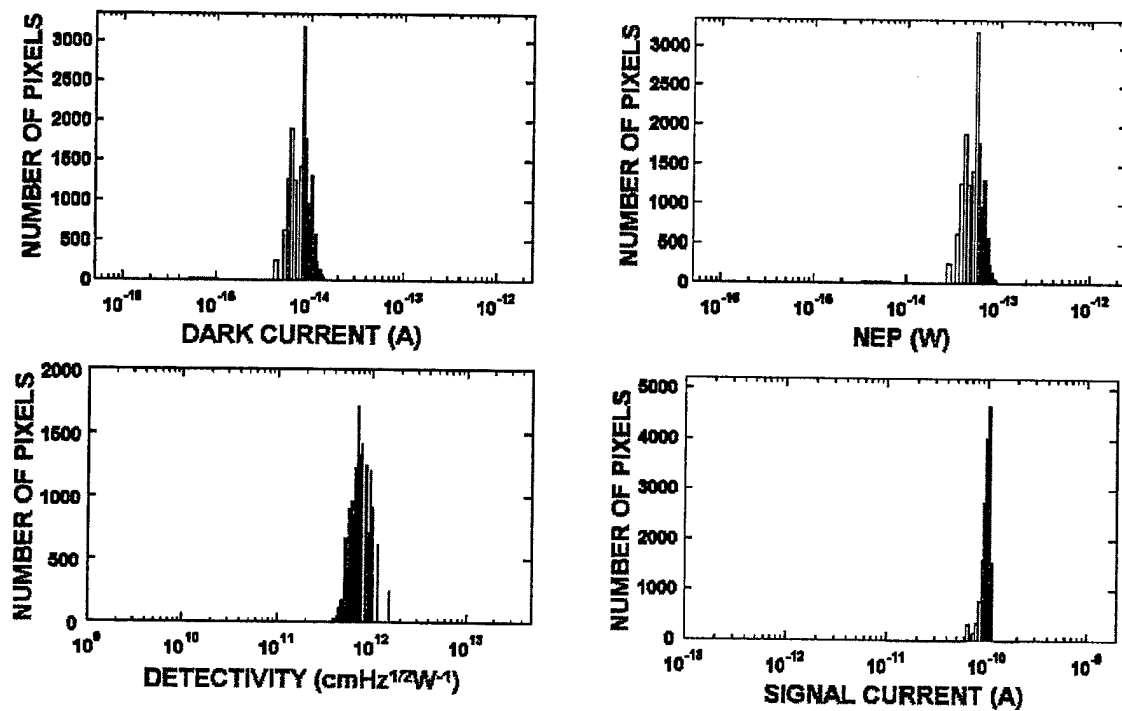


Figure 3.25 Dark current, NEP,  $D^*$ , and photocurrent statistics for 128x128 visible-blind FPA.

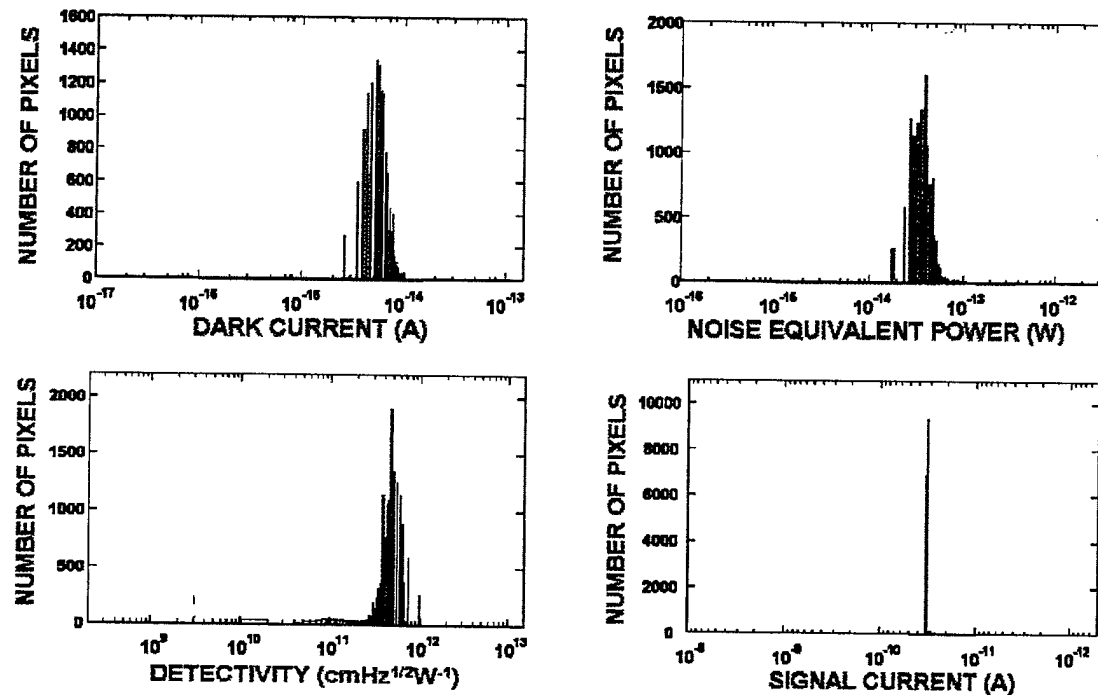


Figure 3.26 Dark current, NEP,  $D^*$ , and photocurrent statistics for 128x128 solar-blind FPA.

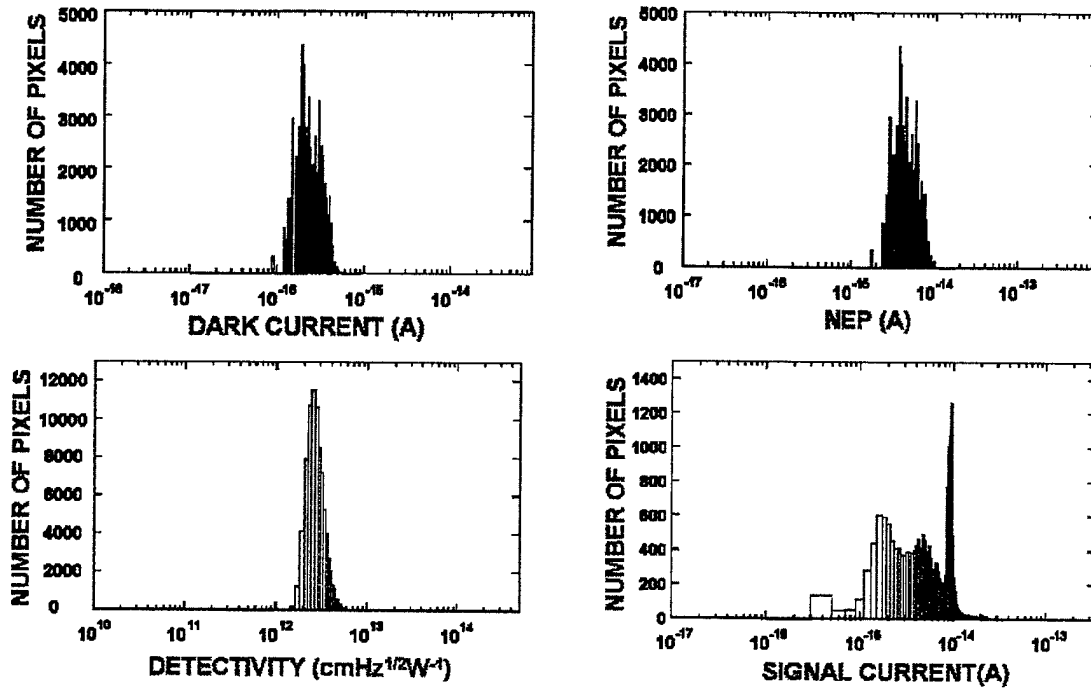


Figure 3.27 Dark current, NEP,  $D^*$ , and photocurrent statistics for 320x256 solar-blind FPA.

Figure 3.24 that the 320x256 ROIC exhibits much smaller dark currents and NEP values compared with the 128x128 array -- by about a factor of fifty. This is expected since the larger ROIC comes with low-noise CTIA input circuitry. The characteristics of the ROICs shown in this figure place an upper bound on the characteristics of the hybridized diode arrays, since even perfect photodiodes (no noise) will exhibit the ROIC noise after hybridization.

Figure 3.25 shows dark current, NEP,  $D^*$ , and photocurrent statistics for a hybridized 128x128 visible-blind FPA. It is seen that the dark current, NEP, and  $D^*$  appear to be somewhat less than corresponding values for the ROIC shown in Figure 3.25. We attribute this to additional noise associated with the floating inputs of the

ROIC of Figure 3.24. Note that the hybridized FPA shows a very narrow photocurrent output when illuminated with moderate UV light.

Figure 3.26 shows dark current, NEP,  $D^*$ , and photocurrent statistics for a hybridized 128x128 solar-blind FPA. Note that the hybridized solar-blind array exhibits properties very similar to the hybridized visible-blind device of Figure 3.25. We believe this is the case because both of the hybridized arrays that employ 9806 ROICs are being limited by the noise properties of the ROIC. Recall, that individual visible-blind diodes and solar-blind diodes exhibit  $D^*$  values much higher than those obtained for the corresponding hybridized arrays.

Additional evidence for the above interpretation is provided by the 320x256 array statistics shown in Figure 3.27. This array was made from the same wafer as the 128x128 solar-blind array of Figure 3.26. Note, however, that the 320x256 array exhibits smaller dark currents, NEP values, and  $D^*$  values by approximately a factor of fifty -- due, it is believed, to the low-noise CTIA input of the 9809 ROIC.

It seems clear from the results that have been obtained that, at present, the AlGaN photodiodes have extremely desirable properties for UV FPA applications. However, to fully realize their potential, very low noise silicon ROICs may have to be developed.

#### 4. SUMMARY

The goal of this research program was to develop high quality III-V nitride materials and to use them to make photodiode arrays that can then be used for imaging applications. GaN and AlGaN materials were grown by MOVPE on double-side-polished sapphire substrates and characterization results used to optimize the growth process. Characterization experiments included optical measurements to observe the absorption edge (cathodoluminescence and transmittance measurements), and electrical C-V measurements to determine for the carrier concentration. The devices were developed to have detection windows in the visible-blind UV region (300 nm to 365 nm) and also the solar-blind region (240 nm to 285 nm). Photodiodes were fabricated from these samples for the purpose of studying the diode characteristics and also their spectral responsivity. Devices with high quantum efficiency were observed.

Arrays of photodiodes were then fabricated and hybridized to matching ROIC using Indium bump bonds. They were then mounted in a special digital camera and a number of UV images and movies made with both the solar blind and visible blind arrays. These UV arrays were observed to have a high degree of uniformity and a high degree of pixel activation.

It was also observed that the silicon ROICs employed were the limiting factor in the performance of the hybridized FPAs. The 128x128 arrays, which were hybridized to 9806 ROICs having direct injection input circuitry, adversely affected the noise performance of the hybridized devices. Photodiode arrays hybridized to

320x256 9809 ROICs, which had CTIA imput circuitry, had improved noise performance.

During the course of the work presented here, high quality GaN and AlGaN materials were developed, but there is still room for increasing their quality. Optimization of the various layers of the device structures, and improving the quality of the AlN buffer layer, would help in further improving the surface morphology.

Another area of future work could be to improve the ROIC design so that smaller signals could be detected. The ROICs used in this work were basically designed for imaging in the infrared region. However, new ROICs will need to be designed around the properties of the UV photodiodes in order to fully realized their potential.

With further development, these new UV-specific digital images may find widespread use in the areas of welding imagery, flame sensing, medical imagers, biofluorescence imaging, atmospheric ozone detection and analysis of crime scenes in addition to providing very sensitive imaging systems for missile threat warning applications.

## 5. REFERENCES

- [1] Shuji Nakamura, Takashi Mukai, Masayuki Senoh, *Appl. Phys. Lett.* 64, 1687-1689 (1994)
- [2] Shuji Nakamura, Masayuki Senoh, Naruhito Iwasa, Shin-ichi Nagahama, *Appl. Phys. Lett.* 67, 1868-1870 (1995)
- [3] S. Nakamura, M. Senoh, S. Nagahama, N. Iwasa, T. Yamada, T. Matsushita, Y. Sugimoto, H. Kiyoku, *Appl. Phys. Lett.* 70, 1417-1419 (1997)
- [4] Shuji Nakamura, Gerhard Fasol, *The Blue Laser Diode – GaN based Light Emitters and Lasers* (Springer-Verlag, Heidelberg, 1997)
- [5] F.A. Ponce, *MRS Bull.* 22, 51-57 (1997)
- [6] J. Edmond, H.S. Kong, M. Leonard, G. Bulman, G. Negley, *Inst. Phys. Conf. Ser.* 142, 991 (1996)
- [7] I. Akasaki, S. Sota, H. Sakai, T. Tanaka, M. Koike, H. Amano, *Electron. Lett.* 32, 1105-1106 (1996)
- [8] G.E. Bulman, K. Doverspike, S.T. Sheppard, T.W. Weeks, H.S. Kong, H.M. Dieringer, J.A. Edmond, J.D. Brown, J.T. Swindell, J.F. Schetzina, *Electron. Lett.* 33, 1556-1557 (1997)
- [9] M.P. Mack, A. Abare, M. Aizcorbe, Peter Kozodoy, S. Keller, U.K. Mishra, L. Coldren, Steven DenBaars, *MRS Internet J. Nitride Semicond. Res.* 2,41 (1997)
- [10] S. Nakamura, M. Senoh, S. Nagahama, N. Iwasa, T. Yamada, T. Matsushita, Y. Sugimoto, H. Kiyoku, Y. Sugimoto, T. Kozaki, H. Umemoto, M. Sano, K. Chocho, *Appl. Phys. Lett.* 72, 211-213 (1998)
- [11] D.K. Wickenden, K.R. Faulkner, R.W. Brander and B.J. Isherwood, *J. Cryst. Growth*, 9, 158 (1971)
- [12] S.L Chuang, *Physics of Optoelectronic Devices*, Wiley, New York (1995).

[13] The Book of Photon Tools, p. 1-25, distributed by Oriel Corporation, available through the World Wide Web at <http://www.orient.com>.

[14] Wei Yang, Thomas Novova, Subash Krishnankutty, Robert Torreano, Scott McPherson, Holly Marsh, Appl. Phys. Lett. 73, 1086 (1998)

[15] J.W. Huang, T.F. Kuech, Hongqiang Lu and Ishwara Bhat, "Electrical Characterization of Mg-doped GaN grown by Metalorganic Vapor Phase Epitaxy", Appl. Phys. Lett. 68, 2392 (1996).

[16] E.Schibli and A.G. Milnes, "Effects of Deep Impurities on n+p Junction Reverse-biased Small Signal Capacitance", Solid-State Electron. 11, 323 (1968).